

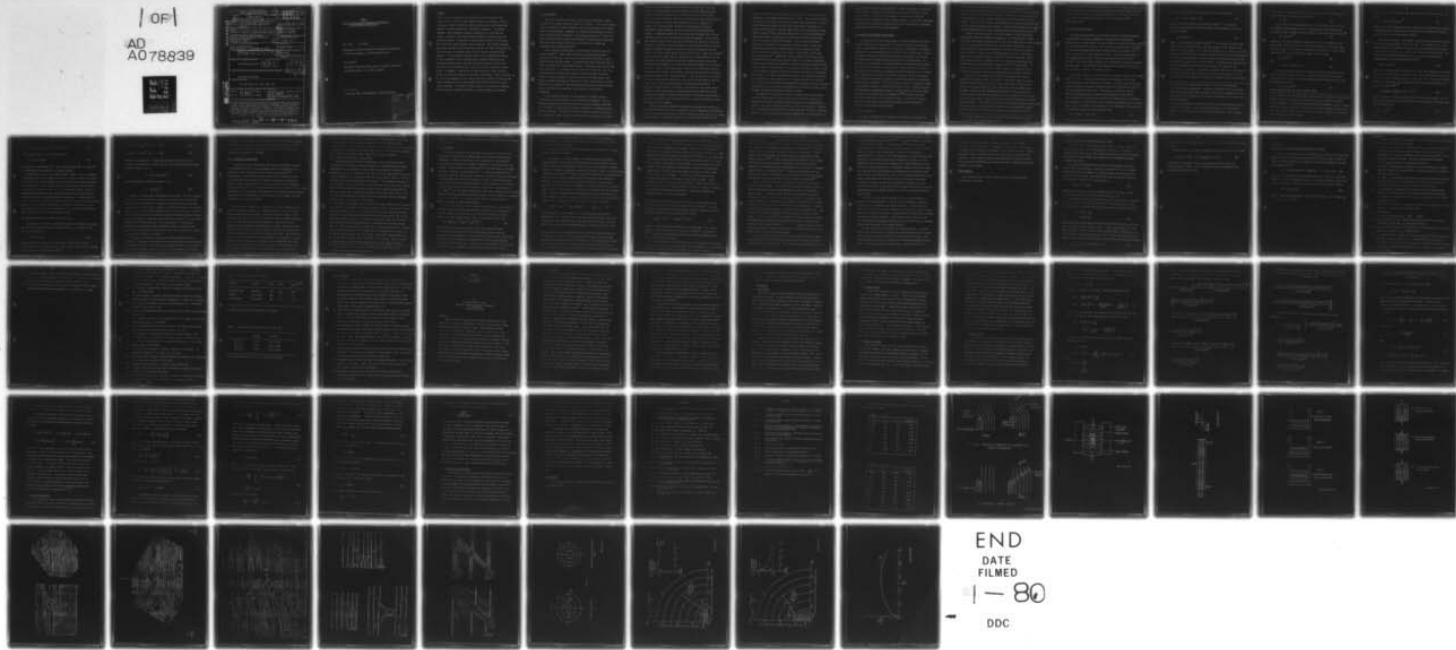
AD-A078 839 CALIFORNIA UNIV BERKELEY DEPT OF MATERIALS SCIENCE A--ETC F/G 11/2
ELASTIC/PLASTIC INDENTATION DAMAGE IN CERAMICS. I. THE MEDIAN/RA--ETC(U)
DEC 79 B R LAWN , A G EVANS , D B MARSHALL N00014-79-C-0159

UNCLASSIFIED

1 OF 1

AD
AO78839

NL



END

DATE

FILMED

1-80

DDC

1032-594
READ INSTRUCTIONS BEFORE COMPLETING

REPORT DOCUMENTATION PAGE		
REPORT NUMBER 6	2. GOVT ACCESSION NO.	3. RECIPIENT'S CATALOG LEVEL
4. TITLE (Include Subtitle) Part I. Elastic/Plastic Indentation in Ceramics. I. The Median/Radial Crack System. Part II. A Study of Kink Band Formation in Composites.		
5. TYPE OF REPORT & PERIOD COVERED Jan. 1, 1979 - Dec. 1, 1979		
6. PERFORMING ORG. REPORT NUMBER 10		
7. CONTRACT OR GRANT NUMBER N00014-79-C-0159		
8. PERFORMING ORGANIZATION NAME AND ADDRESS Materials Science and Mineral Engineering University of California Berkeley, CA 94720		
9. PROGRAM ELEMENT, PROJECT, TASK AREA & WORK UNIT NUMBERS 11 1 Dec 79		
10. CONTROLLING OFFICE NAME AND ADDRESS Office of Naval Research 800 N. Quincy St. -- Arlington, VA 22217		
11. REPORT DATE		
12. NUMBER OF PAGES		
13. SECURITY CLASS. (of this report) Unclassified		
14. MONITORING AGENCY NAME & ADDRESS (if different from Controlling Office) (9) Rept for 1 Jan - 1 Dec 79		
15a. DECLASSIFICATION/DOWNGRADING SCHEDULE		
15. DISTRIBUTION STATEMENT (of this Report) Distribution unlimited		
16. DISTRIBUTION STATEMENT (of the abstract entered in Block 20, if different from Report) Distribution unlimited		
17. SUPPLEMENTARY NOTES To be published in Jnl. Amer. Ceram. Soc.		
18. KEY WORDS (Continue on reverse side if necessary and identify by block number) (Part I): B.R. Lawn, A.G. Evans & -- indentation, cracks, residual stresses, fracture toughness. (Part II): A.G. Evans & C.H. Hseuh -- kinking, composites, carbon-carbon, shear bands, inhomogeneities, shear strength		
19. ABSTRACT (Continue on reverse side if necessary and identify by block number) (I) A theory for describing the evolution of the median/radial crack system in the far field of sharp-indenter contacts is developed. Analysis is based on a model in which the complex elastic/plastic field beneath the indenter is resolved into elastic and residual components. The elastic component, being reversible, assumes a secondary role in the fracture process: although it does enhance downward (median) extension during the loading half-cycle, it suppresses surface (radial) extension to the extent that significant growth		

DDC FILE COPY

PART I.

ELASTIC/PLASTIC INDENTATION DAMAGE IN CERAMICS: I.
THE MEDIAN/RADIAL CRACK SYSTEM

B.R. Lawn* A.G. Evans

Department of Materials Science and Engineering, University
of California, Berkeley, California 94710, U.S.A.

D.B. Marshall

Department of Applied Physics, School of Physics, University
of New South Wales, N.S.W. 2033, Australia

* On study leave, from University of New South Wales

Accession For	
NTIS GRA&I	<input checked="" type="checkbox"/>
DDC TAB	<input type="checkbox"/>
Unannounced	<input type="checkbox"/>
Justification	
By	
Distribution/	
Availability Codes	
Dist	Avail and/or special

A

ABSTRACT

➤ A theory for describing the evolution of the median/radial crack system in the far field of sharp-indenter contacts is developed. Analysis is based on a model in which the complex elastic/plastic field beneath the indenter is resolved into elastic and residual components. The elastic component, being reversible, assumes a secondary role in the fracture process: although it does enhance downward (median) extension during the loading half-cycle, it suppresses surface (radial) extension to the extent that significant growth continues during unloading. The residual component accordingly provides the primary driving force for the crack configuration in the final stages of evolution, where the crack tends to near-half-penny geometry. On the hypothesis that the origin of the irreversible field lies in the accommodation of an expanding plastic hardness impression by the surrounding elastic matrix, the ensuing fracture mechanics relations for equilibrium crack growth are found to involve the ratio hardness-to-modulus as well as toughness. Observations of crack evolution in soda-lime glass provide a suitable calibration of indentation coefficients in these relations. The calibrated equations are then demonstrated to be capable of predicting the widely variable median and radial growth characteristics observed in other ceramic materials. The theory is shown to have a vital bearing on important practical areas of ceramics evaluation, including toughness and strength. ↗

I. INTRODUCTION

The fracture patterns generated by small-scale contact events relate strongly to the general mechanical behavior of ceramics. This is particularly true of contacts with "sharp" indenters, where elastic/plastic stress fields govern crack development: toughness K_c , hardness H and stiffness E then all enter as basic material parameters in the fracture mechanics.^{1,2} Apart from their more direct uses in materials evaluation,^{1,3} sharp-contact indentation techniques have important applications in the fields of strength and strengthening,² erosion⁴ and wear.^{5,6}

Cracks induced by elastic/plastic contact may be classified into two primary systems:^{1,7} those cracks which form on symmetry median planes containing the load axis, and those which form laterally on planes closely parallel to the specimen surface. The present paper deals with the first of these two systems, the "median/radial" system. Cracking of this type has long been recognised in the hardness testing of more brittle materials, by virtue of characteristic surface traces emanating radially from the impression corners. However, quantitative use was not made of such observations until Palmqvist demonstrated that the length of the radial cracks could be related empirically to toughness.⁸ Palmqvist worked exclusively with metal carbides, and his work accordingly received little attention in the ceramics literature.

A more fundamental approach to the median/radial problem, based on Griffith/Irwin fracture mechanics, has recently been developed.¹ Once the underlying indentation driving forces for the fracture have been identified and formulated, this approach provides the framework for a complete analysis of crack evolution: in particular, specific relations for crack dimensions as a function of contact load may be determined, with toughness K_c and other

material parameters entering the description in a natural way. The first study along these lines was by Lawn and Swain,⁷ who considered the growth of subsurface median cracks within an essentially elastic point-contact field. Hardness entered the equations via the assumption that some plasticity would be necessary to remove stress singularities at the indenter tip. However, this initial attempt oversimplified the problem by using two-dimensional fracture mechanics to solve an essentially three-dimensional problem. A subsequent study⁹ took into account the observation that all well-developed cracks in point loading tend to penny-like geometry. While noting that residual stresses about the plastic zone must play some role in the crack evolution, particularly in the enhancement of surface radial extension during indenter unloading, the modified analysis retained the assumption that the primary crack driving force derived from the elastic field. Evans and Wilshaw¹⁰ took the analysis a step further by dealing with an elastic/plastic field from the outset, and thereby maintained that the hardness-to-modulus ratio, H/E , should complement toughness as a controlling material parameter in the fracture mechanics. However, these workers used a semi-empirical dimensional analysis to formulate their theory, thus avoiding a detailed description of the physical mechanisms responsible for fracture evolution. Evans and Wilshaw also extended the range of experimental observations, previously confined almost exclusively to the "model" material soda-lime glass, to polycrystalline ceramics. A principal finding here was a transition in the pattern of crack growth toward dominance of the surface radial component relative to the subsurface median in the earlier stages of loading as the ratio H/E diminished, notwithstanding the fact that the same, near-semicircular profile is almost invariably attained upon removal of the indenter.

While these fracture mechanics investigations provided some indication of the role of plasticity in crack propagation, the only quantitative information came from strength-test procedures in which indentation methods were used to emplace starting flaws.¹¹ From these procedures it was found that toughness values

evaluated from crack-size measurements were consistently smaller than those determined by independent means (typically by $\approx 30\%$). This discrepancy could be removed by polishing or annealing the indented test-piece before breaking. It was therefore concluded that the newly formed plastic impression in a contact event must exert a residual opening force on the accompanying cracks. Marshall and Lawn¹² duly incorporated this effect into a more comprehensive indentation analysis, giving explicit recognition to elastic and residual terms in the stress intensity formulation. The new analysis provided a quantitative explanation of the evolution of median cracks in glass, and emphasised the importance of considering the fracture mechanics during unloading as well as loading of the indenter. Application of the results to strength analysis¹³ revealed the residual component of the indentation stress field to be an even more important factor in the growth of degrading flaws than had hitherto been suspected. However, the approach adopted in this work was somewhat phenomenological, with certain indentation parameters in the fracture mechanics equations treated as adjustable constants to be determined empirically for any given indenter/specimen system. An immediate shortcoming of this approach is that observations of fracture evolution in one material are of little value in predicting the prospective performance of other materials; in particular, the theory offers no explanation of why median cracking appears dominant in some cases, and radial cracking in others.

The objective of the present study is to reexamine the elastic/plastic force field responsible for crack extension more critically, and thence to establish a rationale for predetermining the mechanics of the median/radial system for any material whose parameters K_c , H and E are specified. Although it is acknowledged that the question of crack initiation can have an important bearing on the ensuing fracture geometry,¹ attention will be focussed here on

the propagation stage of crack development. Vickers indentations on soda-lime glass provide a reference indenter/specimen system for calibration purposes; the formulation is then shown to be capable of predicting all essential features of crack evolution in other selected materials. In the model developed here the role of the elastic component of the crack driving force is completely subordinate to that of the residual component.

II. MODEL OF MEDIAN/RADIAL CRACK SYSTEM

All indentation fracture analyses begin with some knowledge of the stress fields through which the cracks evolve.¹ If an exact solution for any given contact configuration is available it is possible, in principle, to determine the mechanics of crack development at all points of the loading cycle. However, the general complexity of elastic/plastic contact fields makes it necessary to introduce several simplifying approximations into the description. For instance, it is convenient to distinguish between the near field and far field about the deformation zone. The more complex question of crack initiation, so sensitive to the strongly inhomogeneous stress distributions in the vicinity of the elastic/plastic boundary, can then be separated out from the problem, and the ensuing propagation accordingly treated without specific consideration given to details of contact.¹ While the initiation stage is certainly important in determining thresholds to fracture,¹⁴ and may well be a controlling factor in establishing the dominance of either a surface radial or subsurface median component in the earlier stages of propagation,^{15,16} the model developed here will pertain only to "well-developed" cracks. In this way it becomes possible to treat the median and radial extensions self-consistently in terms of a single-plane fracture system.

(1) The Basic Model

The major simplifying step in setting up the model is to subdivide the

net indentation driving force for the fracture into well-defined components, and then make use of the additive properties of stress intensity factors.¹⁷ This is done according to the scheme of Marshall and Lawn,¹² in which the elastic/plastic field of the fully loaded indenter is considered as the superposition of the residual field in the unloaded solid plus the field of an ideally elastic contact. Implicit in this scheme is the assumption that reversed plasticity does not occur during unloading of the indenter, a condition which should be satisfied to good approximation by the hard ceramic materials of special interest here.¹⁸

Figure 1 outlines the model. In (a) the indenter at load P generates a median-plane crack of characteristic dimension c . The plastic zone is taken to support the indenter, included angle 2ψ , over the characteristic contact dimension a , and to extend radially outward over a characteristic dimension b . Since the main concern is with crack propagation in the far-field of the contact it is not necessary to specify the detailed geometry of the zone. The diagram shows only the downward dimension of the crack; however, the symbol c may be used to denote any polar dimension within the crack plane, most notably the surface radial and subsurface median dimensions c^R and c^M respectively. It should also be borne in mind that a Vickers indenter will generally induce two mutually orthogonal median-plane crack systems of comparable dimensions.

Separation of the elastic/plastic problem into elastic and residual components is depicted in Figs. 1(b) and (c). The elastic field is taken to operate outside the plastic zone, i.e. in the region where cracking occurs,* reaching its maximum intensity at full loading and reversing completely on unloading. Because of this reversibility the elastic driving force may be characterised by the stress distribution $\sigma(r,\phi)$ at $r \geq b$ (see Fig. 1b) over the prospective crack plane,¹⁷ and may therefore be obtained from classical elastic contact solutions. The residual field arises from mismatch tractions exerted on the surrounding matrix by deformed material within $r \leq b$; this component reaches maximum intensity at full loading, but persists as the indenter is removed.

* Microscopic observation of the radial cracks show that fracture does not extend back into the deformation zone.¹⁰

In the approximation of well-developed cracks, i.e. $c \gg b$, these mismatch tractions manifest themselves as a net outward force acting at the crack center (Fig. 1c). It may be seen from Fig. 1 that adding configuration (b) to configuration (c) is equivalent to reloading the indenter to the original maximum load configuration (a).

(2) Stress Intensity Factors

In writing down expressions for the stress intensity factors appropriate to the elastic and residual components of the composite elastic/plastic indentation crack system Marshall and Lawn made use of two empirical observations:¹²

- (i) the indentation field satisfies the requirements of geometrical similitude,
- (ii) the fully developed median/radial fractures satisfy the relation $P/c^{3/2} = \text{const.}$ appropriate to center-loaded penny cracks.

From these observations it was concluded that the stress intensity factors must both be of the form $K = X P/c^{3/2}$, with the X terms constants to be determined for any given indenter/specimen system. It is pertinent now to examine this conclusion in terms of a more analytical treatment of the model in Fig. 1.

(A) *Residual Component:* Consider first the indented surface in the unloaded state, Fig. 1(c). To evaluate the residual field component the following sequence of hypothetical operations is performed. (i) Begin with an *unstressed* elastic half-space, and remove a segment of material, characteristic radius b , from the prospective contact site. (ii) *Plastically* deform the removed segment by indentation over a contact a and penetration d , such that the irreversible strain associated with creation of the impression is accommodated by an expansion in characteristic zone dimension, at constant volume of material. Then if δV is the volume of the impression and V is the volume of the zone, the configurational strain is of the functional form

$$\delta V/V \sim a^2 d/b^3 \sim (a/b)^3 \cot \psi \quad (1)$$

(iii) *Elastically* restore the segment to its original characteristic radius b

by applying a hydrostatic compression across the outer boundaries,

$$p_3 \sim \kappa(\delta V/V) \sim E(a/b)^3 \cot \psi \quad (2)$$

where κ is the bulk modulus and E the Young's modulus.* This pressure is to be distinguished from that which obtains at the impression at load P , i.e. the hardness,

$$p_a = P/\alpha_0 a^2 \equiv H \quad (3)$$

where α_0 is a geometrical indenter constant.** (iv) Reinsert the pressurised segment into the original cavity, restoring coherence at the interface, and allow the system to relax. It is clear from analogy with the internal spherical inclusion problem¹⁹ that the constraining pressure exerted on the relaxed segment will remain compressive but will reduce to some fraction of the pressure given in Eq. (2) (to one half in an infinite matrix). Relaxation of the pressure over the surface diametral plane must inevitably modify the stresses at the elastic/plastic interface. Consequently, the plastic zone can be considered as a source of effective outward residual force on the crack shown in Fig. 1(c); the magnitude of this force may be obtained by integrating the horizontal stress

* Throughout this analysis terms in Poisson's ratio will be neglected, to avoid unnecessary complication. Empirical justification for this omission comes from the observation that "universal" curve fits to indentation data are insensitive to the relatively small variations in Poisson's ratio which occur in different ceramics.³

** In this work hardness is defined in terms of the projected rather than the actual area of contact. Thus for pyramid indenters $\alpha_0 = 2$, which differs slightly from the value used in evaluating the conventional Vickers hardness number.

components over the zone cross section within the crack plane, assuming p_b to remain effectively invariant with crack size,*

$$P_r \sim p_b b^2 \quad (4)$$

In the limit of well-developed cracks, $c \gg b$, the forces in Eq. (4) may be regarded as concentrated at a point. Assuming penny-like crack geometry, the stress intensity factor due to the residual far-field force may be written²⁰

$$K_r \sim f(\phi) P_r / c^{3/2} \quad (5)$$

where $f(\phi)$ is an angular function introduced to allow for the effects of the free surface; generally $f(\phi)$ is a slowly-varying function, of value near unity, with its minimum at $\phi = 0$ (median orientation) and maximum at $\phi = \pm 90^\circ$ (radial orientation).²⁰ Eqs. (2) to (4) then combine with (5) to give

$$K_r = X_r P / c^{3/2} \quad (6)$$

with

$$X_r \sim f(\phi) (a/b) (E/H) \cot \psi \quad (7)$$

To take the analysis further it is necessary to specify how the ratio a/b varies with indenter/specimen system. A detailed treatment of the analogous expanding cavity problem in an infinite isotropic elastic/plastic matrix, gives the approximate result**

$$b/a \sim (E \cot \psi / H)^{1/2} \quad (8)$$

On the assumption that this result remains a good

* This assumption has some experimental justification.¹² Theoretical analysis (see Appendix A) does in fact show the crack opening force P_r to vary slowly with c .

** See Appendix B. It may also be noted here that the quantity H is not a constant, but depends itself on $E \cot \psi$.²² However, the functional dependence is much slower than linear (logarithmic), in which case H in Eq. (8) may be taken to be suitably represented by the Vickers hardness.

approximation for the equivalent half-space problem, substitution into Eq. (7) gives

$$X_2 = \xi_r^{1/2} (\phi) [(E/H) \cot \psi] \quad (9)$$

where $\xi_r(\phi)$ is now a dimensionless term *independent* of indenter/specimen system.

In accordance with the median/radial dichotomy the two quantities ξ_r^M and ξ_r^R (with $\xi_r^R > \xi_r^M > 0$) are of particular interest.

(B) *Elastic component*: Now consider the contribution to the crack driving force from the elastic matrix itself, Fig. 1(b). As indicated in Sect. II(1), this component can be evaluated in terms of the *prior* elastic contact stresses over the crack plane, at $r \geq b$. Since it is the far-field solution which is of concern here the stress distribution, at $r \gg a$, may be most conveniently represented by the point-load Boussinesq result⁷

$$\sigma(r, \phi) \sim g(\phi) P/r^2 \quad (10)$$

where $g(\phi)$ is another angular function; in this case $g(\phi)$ appropriate to stresses normal to the median plane is strongly varying, changing from positive (tensile) at $\phi = 0$ to negative (compressive) at $\phi = \pm 90^\circ$ (Fig. 1b). The stress intensity factor for a half-penny crack subjected to radially distributed stresses over $b \leq r \leq c$ is given by^{20,21}

$$K = f(\phi) (2/c)^{1/2} \int_b^c r \sigma(r) dr / (c^2 - r^2)^{1/2} \quad (11)$$

Ignoring effects due to the $g(\phi)$ functional variation for the present, Eq. (9) may be substituted into the integral to yield an elastic stress intensity factor of the familiar form

$$K_e = X_e P/c^{3/2} \quad (12)$$

where

$$X_e \sim f(c) g(\phi) \ln\{(c/b)[1 + (1 - b^2/c^2)^{1/2}]\}. \quad (13)$$

In the required limit $c \gg b$, Eq. (13) reduces to

$$X_e = \xi_e(\phi) \ln(2c/b) \quad (14)$$

where $\xi_e(\phi)$ is another global term. Again, ξ_e^M and ξ_e^R (with $\xi_e^M > 0$ and $\xi_e^R < 0$) are identified as key constants in the present analysis.

The parameter X_e in Eq. (14) warrants further comment. First, it contains a logarithmic term in crack length, so the stress intensity factor in Eq. (12) is not strictly of the simple centre-loaded penny form assumed in previous studies. On the other hand, over the typical range of indentation sizes encountered in the testing of ceramics, $1 < c/b < 10$, X_e is not strongly varying. Second, in integrating the stress distribution over the prospective crack plane improper allowance was made for variations along the ϕ -coordinate: to regard $\xi_e(\phi)$ in Eq. (14) as being determined by the product $f(\phi)g(\phi)$ is a clear oversimplification. However, it will be argued later that K_e is secondary in importance to K_r in determining the ultimate crack configuration; in this light the approximations made in deriving Eq. (14) are not considered critical.

(3) Equilibrium Relations for Median and Radial Cracks

The condition for equilibrium growth of the cracks is obtained by equating the net stress intensity factor, K , to the toughness, K_c . For the system in Fig. 1 this condition is

$$K = K_e + K_r = K_c. \quad (15)$$

Bearing in mind the reversibility of the elastic term, Eq. (12), and the irreversibility of the residual term, Eq. (6), separate equations may be written for the loading and unloading half-cycles:¹²

$$X_e P/c^{3/2} + X_r P/c^{3/2} = K_c \quad (P \uparrow) \quad (16a)$$

$$X_e P/c^{3/2} + X_r P_* / c^{3/2} = K_c \quad (P \downarrow) \quad (16b)$$

where P_* is the peak load. If the crack maintains a semicircular front throughout its evolution, it follows from Eq. (16) that the equilibrium radius at maximum load $P \uparrow = P_*$ is

$$c_* = [(X_e + X_r) P_* / K_c]^{2/3} \quad (17a)$$

and correspondingly at complete unload $P \downarrow = 0$ is

$$c_\dagger = (X_r P_* / K_c)^{2/3}. \quad (17b)$$

However, two factors need consideration at this point. The first concerns the practical fracture conditions under which the requirements of mechanical equilibrium can be maintained. In particular, crack growth is not generally reversible, so Eq. (17b) cannot represent an attainable equilibrium configuration unless $c_\dagger > c_*$. For the median component, $X_e^M > 0$, so the only way of realising this inequality is somehow to suppress crack growth during the loading half-cycle (e.g. by superposing a reversible surface compressive stress).¹² For the radial component, on the other hand, $X_e^R < 0$, so the inequality is automatically satisfied. Thus the median crack is expected to attain its maximum growth during the loading half-cycle, whereas the radial crack is expected to continue its growth until unloading is complete.

The second factor concerns the angular variations inherent in the X parameters. These angular variations are of course manifest in the identification of the median and radial crack components as separate entities in the evolution. Direct insertion of Eqs. (9) and (14) into (16) cannot therefore be expected to provide a highly accurate representation of the growth history at those stages

where departures from radial symmetry within the crack plane are most apparent. Fortunately, the problem is minimal in the configuration which is ultimately of greatest concern, namely that at full unloading, where the tendency to ideal penny-like geometry is strongest.

III. EXPERIMENTAL OBSERVATIONS

The evolution of the median/radial crack system was monitored optically. For transparent materials, crack development could be followed *during* the indentation cycle, from either the side or below the specimen.^{10,12} Alternatively, a useful record of crack history could, in favorable cases, be reconstructed *after* indentation by examining fractographic features on specimens subsequently made to fail from one of the two mutually orthogonal half-pennies (Fig. 2).¹² In all cases the loading cycle was carried out in an inert environment (e.g. dry nitrogen gas or paraffin oil) to maintain near-equilibrium conditions in the crack growth, and with a Vickers pyramid indenter to ensure reproducibility in the crack pattern.

Soda-lime glass, because of its transparency, isotropy, homogeneity and general availability, was used as a reference material in the present study. Indentation-load/crack-size results, suitably normalised to produce linear, universal plots for all peak loads, are shown for median and radial components in Fig. 3: the data points represent experimental observations made on several cracks, and the solid lines represent curve fits. Under normal test conditions, data could be obtained for medians only during the loading half-cycle, and for radials only during the unloading half-cycle. The median data at $P_f = 0$ in Fig. 3 were derived from a contrived test arrangement in which a reversible flexural stress was superimposed on the indentation field; this closure stress suppressed growth during loading to the extent that $c_*^M < c_f^M$ (Sect. II(3)), thereby producing a final equilibrium crack configuration equivalent to that which would have obtained under normal circumstances had

cycle would have required loads in excess of the maximum used here, in order to enforce propagation of the expanding, subsurface crack to the free surface ("breakthrough").⁷ The indentation coefficients in Eq. (16) now follow directly from the slopes and intercepts of the fitted lines in Fig. 3: for the median component, $x_e^M = 0.032 \pm 0.008$ and $x_r^M = 0.026 \pm 0.003$;¹² for the radial component, $x_e^R = -0.045 \pm 0.002$ and $x_r^R = 0.049 \pm 0.004$.

The determination of reference coefficients in this way affords a useful "calibration" of the fracture mechanics equations for the median/lateral system; predictions of crack evolution can now be made for any material of specified parameters K_c , H and E . According to Eq. (14), the coefficients pertaining to the elastic component of the indentation field involve only spatial factors, in which case x_e^M and x_e^R should be the same for all materials.* The residual component, on the other hand, is seen from Eq. (9) to be material-sensitive; evaluation of x_r^M and x_r^R for different specimens accordingly requires specification of appropriate s_r terms in this equation. With the value of E/H for glass taken from Table 1, and $\psi = 74^\circ$ the characteristic half-angle for Vickers indenters, the values obtained are $s_r^M = 0.014 \pm 0.001$ and $s_r^R = 0.026 \pm 0.002$.

Indentation fracture data were collected for two other materials, zinc sulphide and silicon, to investigate the effect of changing E/H ratio. The results for zinc sulphide are shown in Fig. 4. This time the solid lines are *a priori* predictions from Eq. (16), using the calibrated coefficients above along with Eq. (9) and the material parameters in Table 1. Of special interest here is the enhanced radial crack growth during the loading half-cycle in comparison with the glass results (Fig. 3). This follows directly from Eq. (17a): increasing E/H expands x_r relative to x_e , thereby "washing out" to some extent the strong angular factor inherent in the elastic coefficient (cf. Eqs. (9) and (14)). With silicon, measurements were made of the crack dimensions only at full load and full unload. Table 2 compares the measured dimensions with those predicted from Eq. (17), again using the

* Actually, the elastic stress field does depend on Poisson's ratio,⁷ the effects of which have been neglected here.

calibrated coefficients. Notwithstanding certain discrepancies in the earlier stages of crack evolution the theory appears to be consistent with the calibrated coefficients.

IV. DISCUSSION

The fracture mechanics model presented here provides the framework for a quantitative analysis of the median/radial crack system in elastic/plastic indentation. Central to the analysis is the separation of the indentation force field into "elastic" and "residual" components, as characterised by the X terms. For materials such as soda-lime glass at the high end of the hardness-to-modulus spectrum, i.e. approaching $H/E = 1$, these two components are of comparable magnitude. However, being reversible, the elastic driving force takes on a subordinate role in the crack evolution: whereas it does enhance crack growth in the subsurface median orientation, it serves merely as a restraining influence on the growth in the surface radial orientation. Moreover, since $X_r \sim (E/H)^{1/2}$, while X_e remains effectively constant over the load range of practical indentation testing, the residual component becomes even more dominant as hardness-to-modulus diminishes. It is evident that deformation processes become a controlling factor in sharp-contact fracture.

The fact that the radial crack configuration satisfies the requirements of mechanical equilibrium throughout the entire indentation cycle, approaching its final crack size on unloading, is of special significance in ceramics testing. Eq. (17b) then applies, so that, in conjunction with Eq. (9),

$$c_{\perp}^R = \{\$_r^R (\cot \psi)^{1/2} [(E/H)^{1/2} / K_c]\}^{2/3} P_*^{2/3} \quad (18)$$

This relation provides a sound physical basis for characterising the indentation fracture from surface-trace measurements alone, an obvious advantage for opaque materials. It may be noted that while several indentation constants need to be specified in the description of full crack evolution, only one, $\$_r^R$, enters in Eq. (18). It may also be noted that Eq. (18) is of the form $P/c^{3/2} = \text{const.}$ appropriate to penny cracks in ideal center loading:

it is the appearance of the quantity E/H , in addition to the toughness K_c , which emerges as the primary manifestation of the elastic/plastic far-field driving force for the fracture.

The results embodied in Eq. (18) have important implications in two major areas of materials evaluation:

(A) *Toughness*: Previous studies, in recognising that sharp-contact damage patterns contain explicit information on the relative susceptibilities of any given material to deformation and fracture, have attempted to construct "universal" diagrams for quantifying mechanical response in terms of characteristic indentation dimensions.^{10, 23} Evans and Charles²⁴ showed that such constructions may be used as a simple yet powerful means for determining the toughness of ceramics. These authors, working with materials whose K_c values had been measured independently, found it necessary to introduce an empirical correction factor in H/E in order to obtain a satisfactory "calibration" of their universal plot. The present analysis serves to establish the Evans-Charles approach on a more fundamental footing, at least in the limit of the far-field approximation. Thus Eq. (18), in conjunction with Eq. (3) at $\alpha = \alpha_*$ and $P = P_*$, gives

$$(K_c/E\alpha_*)^{1/2} (H/E)^{1/2} = 0.028 (c_+^R/\alpha_*)^{-3/2} \quad (c_+^R \geq \alpha_*) \quad (19)$$

using the previously cited values of α_0 , ψ and s_p^R appropriate to Vickers indentations. This differs in form from the expression derived by Evans and Charles only in the exponent of H/E , which they set at 0.4 by curve fitting. Figure 5 is a replot of their universal diagram in accordance with Eq. (19).

Recalling that it is the residual field which determines the final length of the surface radial crack, it becomes imperative to ensure that indentation measurements are made under conditions of true equilibrium before attempting to evaluate toughness from Fig. 5; exposure of the newly formed fracture to a reactive environment may result in considerable extension by slow crack growth,

in which case the value determined will be somewhat less than the true K_c .

(E) *Strength:* For any material which fails from a flaw introduced by elastic/plastic contact, the residual indentation driving force must be taken into account in the assessment of strength. Marshall, Lawn and Chantikul¹ showed that this residual term could account for a strength reduction of $\approx 30\%$, consistent with the observations of earlier workers¹¹ (Sect. I). Working on the tacit assumption that failure occurs from the subsurface location $\phi = 0$, such that a relation of the form Eq. (17a) dictates the starting flaw size in the strength test, these authors also showed that for materials satisfying the inequality $x_r^M > x_e^M/3$ the cracks must undergo some precursor stable growth; i.e. failure is not spontaneous. This result was demonstrated to have important repercussions in the design of high-strength systems. Now in the present study, the conclusion that $x_r^R > x_r^M$ would suggest that failure is more likely to occur at a surface location $\phi = \pm 90^\circ$, in which case a relation of the form Eq. (17b) (more specifically, Eq. (18)) should determine the starting flaw size. The elastic parameter,

x_e^R , does not enter the analysis at all this time, so the condition for the existence of an energy barrier to failure is met automatically. Following the analysis by Marshall et al¹⁴ the strength equation corresponding to flaws induced by indenters of given geometry takes the form

$$\sigma \sim (K_c^4/x_r^4)^{1/3} / P_*^{1/3} \sim [K_c^4 (H/E)]^{1/2} x_r^{1/3} / P_*^{1/3} \quad (20)$$

where Eq. (9) has been used to introduce the H/E dependence. This does not represent a serious modification to the earlier analysis:¹⁴ the relation $\sigma P_*^{1/3} = \text{const.}$ still obtains for any given material, and toughness remains the controlling material parameter.

In any applications of the indentation theory in areas such as those just outlined it is necessary to be aware of some of the departures from the idealised system of Fig. 1 that can occur in practice. For instance, it has been

assumed that material beneath the indenter deforms radially at constant volume. In materials with low values of E/E there is a tendency for displaced material to "pile-up" around the indenter, approaching the "fully plastic" conditions exhibited by most soft metals.²⁵ Other, hard materials with "open" network structures, such as the "anomalous" silicate glasses, tend to accommodate the contact stresses by densification rather than by plastic flow.²⁶ In both of these cases the intensity of the residual driving force on any median/radial cracks must be substantially reduced. Comparative birefringence studies of indentation sites in normal vs. anomalous glasses confirm this expected trend;²⁷ indeed, the driving force for the median/radial system is diminished to such an extent in the anomalous glasses that Hertzian cone cracking becomes the dominant mode of fracture.^{26,27}

Another prospective complication that needs consideration is that of crack-interaction effects. It is implicit in the model developed in Sect. II that the median/radial crack system generates on a single, well-defined symmetry plane. The extent to which this picture represents a true crack configuration depends in part on the initiation history. For instance, with Vickers indentations at loads just above threshold, radial cracks may be seen emerging from just two, or three, corners;¹⁶ clearly, development of cracking on one plane impedes development on a second, mutually orthogonal plane. Also, where radial and median components initiate as separate entities, as they appear to do in zinc sulphide,¹⁰ coalescence into a single system may involve a mechanism of step formation where crack overlap occurs, thereby locally pinning the outward-expanding front. However, these disruptions are likely to become of secondary importance as an increasing load drives the cracks outward into a well-developed system.

More severe disruptions may occur in situations where alternative crack systems become unusually active during the indentation, thereby interfering directly with median/radial growth. Thus in the case of the anomalous glasses,

dominant cone fracture provides confining boundaries for any surface radials or subsurface medians that may form.^{9,26,27} An analogous effect is also seen in "normal" soda-lime glass: Kirchner and Gruver²⁸ observed in impact experiments that the median-plane cracking occurs only in a shallow surface region at elevated target temperatures. Although this observation is commensurate with a transition from median-dominated to radial-dominated crack growth due to a diminishing ratio E/E as temperature increases, it is not immediately clear why the surface segments did not expand downward into the familiar half-penny configuration on unloading. However, Kirchner and Gruver also noted that the radial segments were accompanied by particularly large lateral cracks; the implication is that in this instance the expansion of the laterals preceded that of the radials, thus confining the surface crack. Provided due allowance is made for such geometrical variants, e.g. by a suitable recalibration of the basic fracture mechanics relations, the general applicability of the indentation method as a tool for materials evaluation remains intact.

One point not given explicit attention here, but which emerges in a natural way from the analysis, is the role of the characteristic indenter half-angle ψ as a variable in the fracture mechanics. From Eq. (18), for instance, it is seen that sharper indenters should give rise to larger cracks. However, care should be exercised in attempting absolute predictions concerning the effects of indenter geometry: issues such as elastic recovery of the residual impression, increased probability of pile-up around sharper indenters, have not been considered in the present analysis.

Finally, a comment on terminology may be appropriate here. The terms "median" and "radial" used to describe what appears ostensibly to be a single crack system has caused some confusion in the scientific literature. The model outlined above provides a rationale for distinguishing between the two terms. It appears reasonable to suggest that "radial" be used in the

description of any property which relates more closely to the surface dimensions of the crack pattern. The measurement of toughness, and analysis of strength in point contact, as discussed in this section, are cases in point. Conversely, "median" should be used when the crack depth is the controlling dimension. Linear contact situations, e.g. glass cutting, particle abrasion, where the strength-determining crack remains subsurface, afford the best-known examples in this category.

ACKNOWLEDGMENTS

Work funded by the U.S. Office of Naval Research and the Australian Research Grants Committee.

APPENDIX A

Compliance Relations for Median/Radial Crack System

In Sect. II (1)A it was tacitly assumed that the residual crack-mouth opening force P_r (Fig. 1c) is independent of crack size c . In reality, because the compliance of the crack system must increase as fracture proceeds, the effective outward residual force exerted by the deformation zone must correspondingly relax.

This relaxation process may be conveniently represented in terms of a simple linear spring analogue. According to the model of Fig. 1 the central deformation zone may be regarded as a precompressed spring inserted at the mouth of the crack system. The outward force exerted by such an element may be written as a function of wall displacement u_r ,

$$P_r/P_{ro} = 1 - u_r/u_{ro}, \quad (A1)$$

where P_{ro} is the force in the fully compressed state (i.e. at $u_r = 0$) and u_{ro} is the displacement in the fully relaxed state ($P_r = 0$).

A compliance relation for the crack system, giving P_r and u_r as a function of c , is now needed to facilitate evaluation of the required function $P_r(c)$. This relation may be obtained from the standard fracture mechanics equations¹⁷

$$\begin{aligned} G_r &= K_r^2 (1 - v^2)/E \\ &= \frac{1}{2} P_r^2 d\lambda/dc \end{aligned} \quad (A2)$$

with G_r and K_r the crack extension force and stress intensity factor associated with the residual stress component: here $\lambda = u_r/P_r$ is the compliance in the approximation $c \gg b$ and $C = \pi c^2/2$ is the crack-plane area. Inserting Eq. (5) for the residual stress intensity factor (with $\beta \sim f(\phi)$ as the proportionality constant in this equation) into (A2) and integrating gives the compliance relation

$$u_r/P_r = [2\pi(1 - v^2)\beta^2/BE](1 - b/c). \quad (A3)$$

where a condition of zero compliance at $c = b$ is taken as an approximate boundary condition.

The displacement u_r may now be eliminated from Eqs. (A1) and (A3) to obtain

$$P_r = P_{ro}/\{1 + [2\pi(1 - \nu^2) \beta^2 P_{ro}/bEu_{ro}](1 - b/c)\}. \quad (A4)$$

This becomes a relatively slowly-varying function of crack size in the far-field fracture region $c \gg b$. Consequently, P_r may be considered to be effectively constant in eq. (5).

APPENDIX 3

Plastic Zone Characteristics: Expanding Cavity Analogue

Based on a modification of Hill's elastic/plastic analysis of a pressurised, expanding cavity in a isotropic spherical shell,¹⁸ Johnson gives a formulation relating the dimension ratio a/b uniquely to the hardness-to-modulus ratio H/E and indenter angle ψ ;²²

$$H/E = (2/9)\cot\psi\{(a/b)^3[1 + \ln(b/a)^3]\} \quad (1 \leq b/a \leq 2.5) \quad (B1)$$

At $b/a < 1$, the contact is considered "elastic"; at $b/a > 2.5$, it is considered "plastic". Eq. (B1) is plotted in Fig. B1. This complex function is seen to be nearly linear over a wide range of b/a , so that a simple power law relation

$$b/a \sim (E \cot\psi / H)^n \quad (B2)$$

affords a reasonable approximation. The plot of Eq. (B2) in Fig. B2 shows that $n = 1/2$ provides a good fit.

REFERENCES

1. B.R. Lawn and T.R. Wilshaw, "Indentation Fracture: Principles and Applications," *J. Mat. Sci.*, 10 [6] 1049-1081 (1975).
2. B.R. Lawn and D.B. Marshall, "Indentation Fracture and Strength Degradation of Ceramics" in *Fracture Mechanics of Ceramics* (Eds. R.C. Bradt, D.P.H. Hasselman and F.F. Lange), Plenum Press, New York 1978, pp. 205-229, Vol. 3.
3. A.G. Evans, "Fracture Toughness: the Role of Indentation Techniques." A.S.T.M. Special Technical Publication 678, in press.
4. A.G. Evans, "Impact Damage in Ceramics," in *Fracture Mechanics of Ceramics* (Eds. R.C. Bradt, D.P.H. Hasselman and F.F. Lange), Plenum Press, New York, 1978, pp. 303-331, Vol. 3.
5. M.V. Swain, "Microcracking Associated With the Scratching of Brittle Solids," in *Fracture Mechanics of Ceramics* (Eds. R.C. Bradt, D.P.H. Hasselman and F.F. Lange), Plenum Press, New York, 1978, pp. 257-272, Vol. 3.
6. J.D.B. Veldkamp, N. Hattu and V.A.C. Snijders, "Crack Formation During Scratching of Brittle Materials," in *Fracture Mechanics of Ceramics* (Eds. R.C. Bradt, D.P.H. Hasselman and F.F. Lange), Plenum Press, New York, 1978, pp. 273-301, Vol. 3.
7. B.R. Lawn and M.V. Swain, "Microfracture Beneath Point Indentations in Brittle Solids," *J. Mater. Sci.*, 10 [1] 113-122 (1975).
8. S. Palmqvist, *Arch. Eisenhüttenwesen*, 33 [] 629- . (1962).
9. B.R. Lawn and E.R. Fuller, "Equilibrium Penny-like Cracks in Indentation Fracture," *J. Mater. Sci.*, 10 [12] 2016-2024 (1975).
10. A.G. Evans and T.R. Wilshaw, "Quasi-Plastic Solid Particle Damage in Brittle Materials," *Acta Metall.*, 24, 939-956 (1976).
11. N. Inglestrom and N. Nordberg, "The Fracture Toughness of Cemented Tungsten Carbides," *Eng. Fract. Mech.*, 6 [] 597-607 (1974); J.J. Petrovic, R.A. Dirks, L.A. Jacobson and M.G. Mendiratta, "Effects of Residual Stresses on Fracture From Controlled Surface Flaws," *J. Am. Ceram. Soc.*, 59 [3-4] 177-178 (1976).

23. H.P. Kirchner and R.M. Gruver, "Localised Impact Damage in a Viscous Medium (Glass)," in Fracture Mechanics of Ceramics (Eds. R.C. Bradt, D.P.H. Hasselman and F.F. Lange), Plenum Press, New York, 1978, pp. 365-377, Vol. 3.
29. P. Chantikul, D.B. Marshall, B.R. Lawn and M.G. Drexhage, "Contact-Damage Resistance of Partially-Leached Glasses," *J. Am. Ceram. Soc.*, in press.

12. D.B. Marshall and B.R. Lawn, "Residual-Stress Effects in Sharp-Contact Cracking: I. Indentation Fracture Mechanics," *J. Mater. Sci.*, in press.
13. D.B. Marshall, B.R. Lawn and P. Chantikul, "Residual-Stress Effects in Sharp-Contact Cracking: II. Strength Degradation," *J. Mater. Sci.*, in press.
14. B.R. Lawn and A.G. Evans, "A Model for Crack Initiation in Elastic/Plastic Indentation Fields," *J. Mater. Sci.*, 12 [11] 2195-2199 (1977).
15. C.M. Perrott, "Elastic/Plastic Indentation: Hardness and Fracture," *Wear*, 45 [] 293-309 (1977).
16. J. Lankford and D.L. Davidson, "The Crack Initiation Threshold in Ceramic Materials Subject to Elastic/Plastic Indentation," *J. Mater. Sci.*, in press.
17. B.R. Lawn and T.R. Wilshaw, *Fracture of Brittle Solids*: Ch. 3. Cambridge University Press, London, 1975.
18. R. Hill, *The Mathematical Theory of Plasticity*: Ch. 5. Oxford University Press London, 1950.
19. J.D. Eshelby, *in Progress in Solid Mechanics* (Ed. I.N. Sneddon and R. Hill). North-Holland, Vol. 2, p. 89 (1961).
20. G.C. Sih, *Handbook of Stress Intensity Factors*. Institute of Fracture and Solid Mechanics, Lehigh University, Bethlehem, Pa., 1973.
21. A.S. Kobayashi, *in Experimental Techniques in Fracture Mechanics* (Ed. A.S. Kobayashi). Iowa State University Press, Ames, Ia., 1973 pp. 4-37.
22. K.L. Johnson, "The Correlation of Indentation Experiments," *J. Mech. Phys. Solids*, 18 [2] 115-126 (1970).
23. B.R. Lawn and D.B. Marshall, "Hardness, Toughness and Brittleness: An Indentation Analysis," *J. Am. Ceram. Soc.*, in press.
24. A.G. Evans and E.A. Charles, "Fracture Toughness Determinations by Indentation" *J. Am. Ceram. Soc.*, 59 [7-8] 371-372 (1976).
25. D. Tabor, *Hardness of Metals*. Clarendon Press, Oxford 1951.
26. J. Hagan, "Cone Cracks Around Vickers Indentations in Fused Silica Glass," *J. Mater. Sci.*, 14 [2] 462-466 (1979).
27. A. Arora, D.B. Marshall, B.R. Lawn and M.V. Swain, "Indentation Deformation/ Fracture of Normal and Anomalous Glasses," *J. Non-Cryst. Solids*, 31 (3) 915- (1979).

TABLE 1. Parameters of Materials Studied

Material	Comment	E/GPa	H/GPa	$K_c/\text{MPa m}^{1/2}*$
Soda-lime glass	Amorphous	70	5.5	0.75
Silicon	Monocrystal	168	9	0.7
Zinc sulphide	Polycrystal	102	1.9	1.0

* Double-torsion data, dry nitrogen gas environment

TABLE 2. Median and Radial Crack Data* for Silicon (111)

	Computed	Measured
$C_*^{M^3/2} \frac{K_c}{P_*}$	0.063	0.064 ± 0.004
$C_*^R^{3/2} \frac{K_c}{P_*}$	0.014	0.031 ± 0.005
$C_{\pm}^R^{3/2} \frac{K_c}{P_*}$	0.059	0.069 ± 0.006

* Fractographic data (cf. Fig. 3), $P^* = 10-30 \text{ N}$ (13 cracks)

FIGURE CAPTIONS

- 1) Median/radial crack system, showing (a) elastic/plastic configuration at full load subdivided into (b) elastic component at full load plus (c) residual component at complete unload. In this model the indentation load P determines the intensity of the crack driving forces: the elastic component is characterised by the distribution of *prior* stresses $\sigma(r, \phi)$ normal to the crack plane (shown in (b) by means of stress contours in the median plane itself); the residual component is characterised by a residual center-opening force exerted by the radially-expanded plastic zone.
- 2) Half-side view and half-schematic of median/radial crack system in soda-lime glass. Micrograph shows fracture surface of specimens broken at indentation sites - crack arrest markings are introduced to provide record of crack evolution. Note failure origin at surface trace of half-penny.
- 3) Fracture mechanics plots for median and radial evolution in soda-lime glass, dry nitrogen environment. Open symbols designate median cracks, closed symbols designate radial cracks (fractographic data, cf. Fig. 3). Solid lines are fits to Eq. (16). (Note: normalised impression size $\alpha^{3/2} K_c/P_* = 0.008$ at $P_* = 50$ N, so that radial cracks "contained" within the contact zone during loading half-cycle for all P_* values used.)
- 4) Fracture mechanics plots for median and radial evolution in zinc sulphide, oil environment. Solid lines are predictions of calibrated Eq. (16). Data points from direct observation of cracks through specimen wall.
- 5) "Universal" plot of radial crack data for toughness evaluation. Solid line is prediction of Eq. (19). (Note: ZnS and glass data in inert environment, other materials tested in air environment.)
- B1) Plot showing Johnson function, Eq. (B1) (solid curve), and power-law approximation (broken line), for expanding cavity representation of elastic/plastic indentation.

PART II.

A STUDY OF KINK BAND FORMATION
IN COMPOSITES

by

C.H. Hseuh and A.G. Evans

Materials Science and Mineral Engineering
U. C. Berkeley
Berkeley, CA 94720

ABSTRACT

Compression tests conducted on carbon/carbon composites have indicated that kink bands in fiber bundles initiate at microstructural inhomogeneities, particularly interfiber voids. Tests conducted on model monolayer glass fiber/epoxy composites (containing notches to simulate pre-existent voids) indicated that kink formation in the composite and shear band formation in the epoxy exhibit comparable morphological features. This result suggests that shear band propagation may be a precursor to kink formation. Computations of the shear stress field around an elliptical hole loaded at infinity indicated that loci of maximum shear stress approximately coincide with the shear band trajectories; thereby providing evidence for the importance of the shear strength of the material in the evolution of shear and kink bands.

I. INTRODUCTION

Carbon/carbon composites (particularly three dimensional arrays) are attractive materials for high temperature applications. The major advantages of this class of composites include: maintenance of good high temperature mechanical properties (at least, in non-oxidizing conditions) and high strength to weight ratios. Recent work has been devoted to enhancing the mechanical properties of these composites; notably, fiber strengthening by etching, thermal stretching¹, neutron irradiation and boron doping²: the improvement of bonding (between the fiber and the matrix) by surface treatment of the fiber³: void minimization by the introduction of several processing cycles^{4,5}: the development of oxidation resistant coatings. One of the remaining limitations of carbon/carbon composites is their relatively low compressive degradation resistance; a phenomenon related to kink formation in the fiber bundles. Several observations of kinking have been reported in the literature, encompassing an appreciable variety of composite systems. Bader and Johnson⁶ noted the existence of kinks on the compressive side of a carbon/epoxy sample subjected to flexure (a particularly illustrative example of the inferior compressive properties of certain composite systems). Weaver and Williams⁷ observed extensive kinking in a similar system deformed in compression under high hydrostatic confining pressure; while Rice⁸ ascertained that kinking was involved in the compressive response of Kevlar 49/epoxy composites. These initial studies concluded that kinking was a consequence of micro-buckling and involved kink initiation concepts based on the critical stress for beam buckling on an elastic foundation. More recently, studies of kinking in a glass fiber/epoxy system by Chaplin⁹ and of carbon/carbon by Evans and Adler¹⁰ have demonstrated the important influence of initial

inhomogeneities on the kink initiation stress. The resultant kink inclination and kink boundary orientation were also tentatively rationalized by minimizing the plastic work and the elastic strain energy, respectively. A dominant dependence of kink initiation on the shear properties of the matrix (elastic and/or plastic) could be readily deduced from the shear mode of matrix deformation that accompanies kinking. However, little progress was achieved in developing quantitative relations between the kink initiation stress, the magnitude of the initial perturbation and the properties of the composites.

Deliberations of the kinking process in fiber composites suggest two principal mechanisms. An instability in fiber rotation may initiate at a region of pre-existent fiber curvature, leading to large matrix shear strains and eventual fiber fracture (Fig. 1a). This mechanism has recently been analyzed by Budiansky and Drucker¹¹; an analysis that emphasized the importance of the (inelastic) slide modulus of the composite and of the magnitude of the initial fiber misorientation. Alternatively, a shear band may initiate in the matrix at a matrix inhomogeneity, such as a void, and propagate unstably across the fiber bundle. The large shear angles at the shear band boundaries will inevitably produce fiber fracture at the boundaries (Fig. 1b). The intent of the present study is to examine the viability of this latter mechanism of kinking: both in general terms and, in particular, for carbon/carbon composites.

The study consists of observations of kinks in carbon/carbon and both kinks and shear bands in glass/epoxy systems, in order to ascertain the character of the inhomogeneities at typical initiation sites. This will establish a basis for the comparison of shear band and kink morphologies. Calculations of the shear stress distributions around inhomogeneities are

then used to rationalize the observed shear band characteristics. These results will subsequently be used to relate the shear band (or kink) initiation stress to the shear properties of the matrix.

2. EXPERIMENTAL

2.1 Test Samples

Experimental studies have been conducted on both carbon/carbon and glass/epoxy composites. The carbon composites of the type considered in this study consisted of bundles of carbon fibers, arranged in an orthogonal interpenetrating network disposed in a matrix of graphite. Compression samples with dimensions $1 \times 1 \times 4 \text{ mm}^3$ were prepared from larger blocks, such that each sample contained a central fiber bundle (dimensions $0.5 \times 0.5 \times 4 \text{ mm}^3$) oriented along the compressive axis. A low melting point Bi alloy with elastic properties comparable to that of the composite was then used to confine the sample within a cylindrical compressive fixture (Fig. 2a). Samples $2 \times 2 \times 12 \text{ mm}^3$ were also prepared for flexure testing. The samples contained two longitudinal fiber bundles, one on the compressive side and the other on the tensile side (Fig. 2b).

Model composites suitable for direct optical observation were also prepared. These consisted of a monolayer of glass fiber embedded in epoxy. The transparency of the epoxy permitted direct observation of the glass fibers. These composites were prepared by firstly mixing the epoxy constituents in a vacuum chamber in order to eliminate internal voids. Glass fibers $\sim 70 \mu\text{m}$ in diameter were then placed on the epoxy surface. A second layer of epoxy was subsequently poured onto the first layer (Fig. 3). An optimum time for superimposing the second layer ($\sim 1\text{hr}$) occurred when the first layer had sufficiently hardened that disturbance of the glass fiber

arrangement could be averted, but short enough to prevent poor adherence of the two layers. Compression samples with dimensions $5 \times 5 \times 8 \text{ mm}^3$ were then prepared. Notches and/or holes were introduced in the samples (Fig. 4), in order to simulate pre-existent matrix inhomogeneities.

2.2 Mechanical Tests

All tests were conducted on an Instron mechanical testing machine, usually at a crosshead speed of $\sim 10^{-4} \text{ ms}^{-1}$. Failure of the compressed sample occurred primarily by fiber splitting in the absence of lateral constraint (cf ref 7); while kinking was the preferred damage mode when constraints were introduced. A constraining medium consisting of a low melting temperature Bi alloy was thus invariably used, as noted above. Deviations from linearity, corresponding to the onset of kinking, occurred in the carbon/carbon composites at $\sim 50 \text{ MPa}$; the ultimate compressive strength was $\sim 70 \text{ MPa}$. Similar mechanical tests have been conducted on the glass/epoxy composites. The deviation from linearity in these materials corresponds directly with the onset of shear band initiation. The yield stress level depended upon the magnitude and morphology of the initiating notch, and was typically in the range 55 to 70 MPa.

2.3 Damage Observations

After mechanical testing, the alloy used for constraint was melted, and the sample removed. The carbon composites were then vacuum impregnated with epoxy and mechanically polished before observing the damage. In the unidirection compression tests, kinking was always determined to initiate from a void, occurring either between the fiber bundle and the matrix (Fig. 5a) or within the fiber bundles (Fig. 5b). In the flexure tests, kinking invariably

occurred at the location of maximum compressive stress (Fig. 6), with no detectable involvement of a microstructural inhomogeneity. The thicknesses of the kinks were $\sim 14\mu$ and the shear strain within the kink (defined as the displacement of a fiber normalized by the kink thickness) was ~ 1 . The kinks were either in-plane or out-of-plane on a specific section¹⁰. The boundaries of in-plane kinks were relatively well defined, such that the angle between the kink boundary and the compressive axis was $\sim 45^\circ$ to 55° . Partially formed kinks were also detected (Fig. 7). These observations can provide invaluable information about the kink formation mechanism. In the glass/epoxy composites (Figs. 8,9) both the kinking and the shear bands were observed to initiate near the notch tip. The shear band comprised two intersecting orthogonal slip lines, as previously noted by Li et al¹². The angle, θ , between the shear band and the compressive axis was $\sim 30^\circ$ to 45° when the notch was aligned normal to the compression axis, and 30° with the notch parallel to the compression axis. The shear strain in the shear band was determined to be ~ 0.7 .

3. STRESS ANALYSIS

The intent of the analysis is to ascertain the distribution of elastic shear stresses in the vicinity of elliptical holes, in order to identify regions of appreciable stress concentration as potential shear band initiation sites. Also, shear stress trajectories through the locations of maximum stress intensification will be deduced, to provide a comparison with the observed shear band trajectories. For this purpose, consider the shear stress around an elliptical hole in an infinite body subject to unidirectional loading. The geometry of the problem is simplified by

adopting a conformal transformation approach. A function that permits an ellipse, with semi-major and semi-minor axes a and b respectively, to be represented by a unit circle (Fig. 10) is given by;

$$Z = w(\xi) = R\left(\xi + \frac{m}{\xi}\right) \quad (1)$$

where $R = (a+b)/2$, $m = (a-b)/(a+b)$. The stress function is thus

$$\begin{aligned} \phi(\xi) &= \frac{PR}{4} \left[\xi + (2e^{2i\alpha} - m) \frac{1}{\xi} \right] \\ \psi(\xi) &= \frac{-PR}{2} \left[e^{-2i\alpha} \xi + \frac{(me^{2i\alpha} - m^2 - 1)\xi}{(m - \xi^2)} + \frac{e^{2i\alpha}}{\xi(m - \xi^2)} \right] \end{aligned} \quad (2)$$

where α is the angle between the loading axis and the b axis of the ellipse and P is the loading. For loading parallel to the b axis ($\alpha = 0$),

$$\begin{aligned} \phi(\xi) &= \frac{PR}{4} \left[\xi + (2-m) \cdot \frac{1}{\xi} \right] \\ \psi(\xi) &= -\frac{PR}{2} \left[\xi + \frac{1}{\xi(m - \xi^2)} + \frac{(m - m^2 - 1)\xi}{(m - \xi^2)} \right] \end{aligned} \quad (3)$$

The relationship between the stress function and the stress, derived by Muskhelishvili¹³ is:

$$\begin{aligned} \sigma\sigma + \tau\tau &= 4R\phi(\xi) \\ \sigma\sigma - \tau\tau + 2i\rho\theta &= \frac{2\xi^2}{\rho w'(\xi)} [w(\xi)\phi'(\xi) + w'(\xi)\psi(\xi)] \end{aligned} \quad (4)$$

and,

$$\phi(\xi) = \frac{\phi'(\xi)}{w'(\xi)}$$

$$\psi(\xi) = \frac{\phi'(\xi)}{w'(\xi)}$$

where σ_r and σ_θ are the radial and tangential stresses respectively, and σ_θ is the shear stress. R represents the real part, $\underline{\quad}$ represents the complex conjugate. A tedious calculation involving Eqns. (3) and (4) gives;

$$\sigma_\theta - \sigma_r + 2i\sigma_\theta = \frac{2p}{1 - \frac{2m}{\rho^2} \cos 2\theta + \frac{m^2}{\rho^4}} \left\{ \frac{(1-m) \left[m^3 \rho^4 i \theta - (m^2 \rho^2 + \frac{m^4}{\rho^2}) e^{2i\theta} + (m^3 - m \rho^4) + (\rho^6 + m^2 \rho^2) e^{-2i\theta} - m \rho^4 e^{-4i\theta} \right]}{(\rho^4 - 2m \rho^2 \cos 2\theta + m^2)^2} \right.$$

$$- \frac{1}{2} \left[\frac{\left[-m \rho^2 e^{4i\theta} + (2m^2 + \rho^4) e^{2i\theta} - (2m \rho^2 + \frac{m^3}{\rho^2}) + m^2 e^{-2i\theta} \right]}{(\rho^4 - 2m \rho^2 \cos 2\theta + m^2)} \right]$$

$$+ \frac{\left[-3m^3 \rho^2 e^{4i\theta} + (3m^2 \rho^4 + 6m^4) e^{2i\theta} - (9m \rho^6 + 18m^3 \rho^2 + \frac{3m^5}{\rho^2}) + (3\rho^8 + 18m^2 \rho^4 + 9m^4) e^{-2i\theta} \right]}{(\rho^4 - 2m \rho^2 \cos 2\theta + m^2)^3}$$

$$\frac{\left[-(6m \rho^6 + 9m^3 \rho^2) e^{-4i\theta} + 3m^2 \rho^4 e^{-6i\theta} \right]}{(\rho^4 - 2m \rho^2 \cos 2\theta + m^2)^3}$$

$$\frac{\left[-m^4 e^{2i\theta} + (3m^3 \rho^2 + \frac{2m^5}{\rho^2}) - (3m^2 \rho^3 + 6m^4 + \frac{m^6}{\rho^2}) e^{-2i\theta} + (m \rho^6 + 6m^3 \rho^2 + \frac{3m^5}{\rho^2}) e^{-4i\theta} \right]}{(\rho^4 - 2m \rho^2 \cos 2\theta + m^2)^3}$$

$$\frac{\left[-(2m^2 \rho^4 + 3m^4) e^{-6i\theta} + m^3 \rho^2 e^{-8i\theta} \right]}{(\rho^4 - 2m \rho^2 \cos 2\theta + m^2)^3}$$

$$\begin{aligned}
& - \frac{(m-m^2-1) \left[\pi^2 \rho^2 e^{4i\theta} - (2m\rho^4 + 2m^3) e^{2i\theta} + (\rho^6 + 4m^2\rho^2 + \frac{m^4}{\rho^2}) - (2m\rho^4 + 2m^3) e^{-2i\theta} + m^2\rho^2 e^{-4i\theta} \right]}{(\rho^4 - 2m\rho^2 \cos 2\theta + m^2)^3} \\
& + \frac{2(m-m^2-1) \left[-m^3\rho^4 e^{6i\theta} + (3m^2\rho^6 + 2m^4\rho^2) e^{4i\theta} - (3m\rho^8 + 6m^3\rho^4 + m^5) e^{2i\theta} \right]}{(\rho^4 - 2m\rho^2 \cos 2\theta + m^2)^3} \\
& + \frac{2(m-m^2-1) \left[(\rho^{10} + 6m^2\rho^6 + 3m^4\rho^2) - (2m\rho^8 + 3m^3\rho^4) e^{-2i\theta} + m^2\rho^6 e^{-4i\theta} \right]}{(\rho^4 - 2m\rho^2 \cos 2\theta + m^2)^3} \Bigg\}
\end{aligned}$$

The imaginary part of Eqn. (5) then yields a relation for the shear stress, as:

$$\begin{aligned}
\rho\theta &= \frac{\rho}{\left(1 - \frac{2m}{\rho^2} \cos 2\theta + \frac{m^2}{\rho^4}\right)} \left\{ \frac{(1-m)([m(m^2+\rho^4)\sin 4\theta - (\rho^3 + \frac{m^2}{\rho})^2 \sin 2\theta]}{(\rho^4 - 2m\rho^2 \cos 2\theta + m^2)^2} \right. \\
& - \frac{1}{2} \left[\frac{-m\rho^2 \sin 4\theta + (m^2 + \rho^4) \sin 2\theta}{\rho^4 - 2m\rho^2 \cos 2\theta + m^2} \right. \\
& + \frac{\left[m^3\rho^2 \sin 8\theta - m^2(5\rho^4 + 3m^2) \sin 6\theta + m(7\rho^6 + 12m^2\rho^2 + \frac{3m^4}{\rho^2}) \sin 4\theta \right]}{(\rho^4 - 2m\rho^2 \cos 2\theta + m^2)^3} \\
& + \left. \frac{\left[-(3\rho^8 + 12m^2\rho^4 + 8m^4 + \frac{m^2}{\rho^4}) \sin 2\theta \right]}{(\rho^4 - 2m\rho^2 \cos 2\theta + m^2)^3} \right]
\end{aligned}$$

$$\left. \frac{2(m-m^2-1)[-m^3\rho^4 \sin 6\theta + 2m^2\rho^2(\rho^4+m^2) \sin 4\theta - m(\rho^8+3m^2\rho^4+m^4) \sin 2\theta]}{(\rho^4-2m\rho^2 \cos 2\theta+m^2)^3} \right\} \quad (5)$$

For the special case, $m = 0$, i.e., for a circular hole

$$\rho\theta = -\frac{P}{2} \left(1 - \frac{3}{\rho^4} + \frac{2}{\rho^2}\right) \sin 2\theta$$

which coincides with the solution for a circular hole with radius $|\xi| = 1^{1/4}$; thereby providing confirmation of the solution. The stress at the boundary of the elliptical hole, $\rho = 1$, simplifies to $\rho\theta = Q$; consistent with the boundary conditions. The real part of Eqn. (5) for the condition $m = 0$, gives;

$$\rho\rho - \theta\theta = P \left[\frac{1}{\rho^2} + \left(\frac{2}{\rho^2} - 1 - \frac{3}{\rho^4} \right) \cos 2\theta \right] \quad (7)$$

From Eqn. (4),

$$\rho\rho + \theta\theta = P \frac{\left(\frac{\rho^2-2\cos 2\theta}{2}\right)}{\rho} \quad (8)$$

Hence,

$$\theta\theta = \frac{P}{2} \left(1 + \frac{1}{\rho^2}\right) - \frac{P}{2} \left(1 + \frac{3}{\rho^4}\right) \cos 2\theta \quad (9)$$

$$\rho\rho = \frac{P}{2} \left(1 - \frac{1}{\rho^2}\right) + \frac{P}{2} \left(1 - \frac{4}{\rho^2} + \frac{3}{\rho^4}\right) \cos 2\theta$$

which is the circular hole solution for a hole radius $|\xi| = 1^{1/4}$. Inserting various values of m into Eqn. (5) permits the shear stress distribution to be derived for any shape of elliptical hole. For example, $m = 1$ refers

to a slit perpendicular to the loading direction, $m = 0$ is a circular hole and $m = -1$ pertains to a slit parallel to the loading direction.

To determine the location of the stresses with respect to the elliptical hole, the coordinates pertinent to the circular hole must be transformed to the appropriate elliptic geometry, using the following relations:

$$z = R(\rho e^{i\theta} + \frac{m}{\rho} e^{-i\theta}), \quad x = R(\rho + \frac{m}{\rho}) \cos\theta, \quad y = R(\rho - \frac{m}{\rho}) \sin\theta,$$

$$r = R[\rho^2 + \frac{m^2}{\rho^2} + 2m\cos 2\theta]^{\frac{1}{2}}, \quad \theta' = \tan^{-1}(\frac{\rho^2 - m}{\rho^2 + m} \tan\theta) \quad (10)$$

A point with polar coordinate (ρ, θ) referred to the circular hole will correspond to a point (r, θ') with respect to the elliptical hole. The shear stress maxima determined using the above procedure can be connected to generate loci of maximum shear stress. The results are summarized in Tables I and II. The resultant shear stresses and maximum shear stress trajectories are plotted in Figs. 11 and 12 for m values of 0.7 and -0.8. These loci extend outward from a location adjacent to the extremity of the major axis. The loci are inclined to the loading direction at 30° for positive m (axial compression) and at $\sim 30^\circ$ to 60° for negative m (normal compression). These angles compare quite favorably with the shear band inclinations determined experimentally, and with the measurements of other authors^{15,16,17}.

4. SHEAR BAND NUCLEATION

The propagation of shear bands in polymers has been most plausibly analyzed by Argon¹⁸, using a notion originally proposed by Bilby, Cottrell and Swinden¹⁹. The model requires that the stress, strain relation for

the material within the shear band exhibit an upper and lower yield phenomenon. This work softening characteristic could result from slip dissociation of initial shear barriers or from adiabatic heating. The propagation of a shear band with this characteristic occurs unstably (under conditions of constant applied shear stress τ). The consequence of this flow behavior is the existence of zones of relatively high shear resistance τ_u (the upper yield stress) within a zone, distance R_0 , from the shear band tip. If such a band extends without an increase in width, the extension is unstable, in accord with the following relation;

$$\frac{R_0}{c} = 1 - \sin \left\{ \frac{\pi}{2} \left(\frac{\tau_u - \tau}{\tau_u - \tau_l} \right) \right\} \quad (11)$$

where $2c$ is the shear band length and τ_l is the shear resistance in the work softened state. When the high resistance zone is small ($R \ll c, \tau \ll \tau_u$), Eqn. (11) reduces to;

$$\frac{R_0}{c} = \frac{\pi^2}{8} \left(\frac{\tau - \tau_l}{\tau_u - \tau_l} \right)^2 \quad (12)$$

Additionally, if τ_l is small

$$\frac{R_0}{c} = \frac{\pi^2}{8} \left(\frac{\tau}{\tau_u} \right)^2 \left[\frac{1 - 2\tau_l/\tau}{1 - 2\tau_l/\tau_u} \right] \approx \frac{\pi^2}{8} \left(\frac{\tau}{\tau_u} \right)^2 \quad (13)$$

This result is equivalent to that for a mode II crack, wherein the nominal critical mode II stress intensity factor is;

$$K_{IIC} \equiv \tau \sqrt{\pi c} = \tau_u \sqrt{8R_0/\pi} \quad (14)$$

An approximate treatment of shear band evolution can thus utilize the well-known solutions for crack growth. More detailed analyses will require a generalization of Eqn. (11) to conditions of non-uniform shear

stress. The mode II stress intensity factor for a shear crack subject to the applied stress $\tau(x)$ is;

$$K_{II} = \frac{1}{\sqrt{\pi a_0}} \int_{-a_0}^{a_0} \tau(x) \left(\frac{a_0 + x}{a_0 - x} \right)^{\frac{1}{2}} dx \quad (15)$$

where $2a_0$ is the length of the shear crack. Consider, therefore, that a small shear inhomogeneity of magnitude $2a_0$ pre-exists near the tip of the major (void) inhomogeneity associated with shear band initiation (analogous to crack initiation in brittle materials at voids or inclusions²⁰.) The minimum possible shear band nucleation stress will evidently pertain when the shear inhomogeneity coincides with the location of the maximum shear stress concentration near the void tip. Approximating the shear stress in this location by;

$$\tau = \hat{\tau} \cos(\pi x/2x_0) \quad (16)$$

when $\hat{\tau}$ is the peak stress and x_0 is the separation between $\hat{\tau}$ and the void surface (Fig. 12), the mode II stress intensity factor becomes;

$$K_{II} = \frac{\hat{\tau} \sqrt{a_0}}{\sqrt{\pi}} \int_{-1}^1 \cos[(\pi/2)x] (a_0/x_0) \left(\frac{1+x}{1-x} \right)^{\frac{1}{2}} dx \quad (17)$$

$$\equiv \frac{\hat{\tau} \sqrt{a_0}}{\sqrt{\pi}} A(a_0/x_0)$$

Rearranging Eqn. (17) gives;

$$\kappa \equiv \frac{K_{II}}{\hat{\tau} \sqrt{x_0}} = \sqrt{\frac{a_0}{x_0}} A(a_0/x_0) \quad (18)$$

A plot of the normalized stress intensity factor, κ (Fig. 13) indicates that it exhibits a broad maximum as a function of the relative inhomogeneity size a_0/x_0 . The stress intensity factor is thus relatively insensitive to the magnitude of the initial shear inhomogeneity. (This is typical of inhomogeneity problems in non-uniform stress fields.) The prevalent stress intensity factor for shear band evolution is thus the peak value. Equating this peak value to the critical stress intensity factor K_{IIC} (see Eqn. 14), the shear band formation condition becomes;

$$\hat{\kappa} \hat{\tau} \sqrt{x_0} = K_{IIC} \quad (18)$$

where $\hat{\kappa}$ is ~ 1.1 . The peak shear stress is related to the applied stress p_A and to the void shape m by;

$$\hat{\tau} = p_A M_1(m) \quad (19)$$

where $M_1(m)$ is given for the inhomogeneities of principal interest ($m \sim 1$) by the approximate relation;

$$M_1(m) \approx \beta(7m^2 + 4m)$$

where β is a constant. The location of the peak, x_0 , is determined by the void average radius R and by the shape m

$$x_0 = RM_2(m) \quad (20)$$

where $M_2(m)$ is given for the same approximation by;

$$M_2(m) \approx \beta'(m+1)$$

Inserting Eqns. (19) and (20) into Eqn. (18) a critical applied stress p_A^C for shear band formation can be obtained as;

$$p_A^C = \frac{\tau_u \sqrt{8R_0/\pi}}{m \sqrt{R(1+m)}(7m+4)} \quad (21)$$

This value for p_A^C is the minimum possible value, and could be exceeded if a shear inhomogeneity within the requisite range does not occur at the location of peak shear stress around the void. Once initiated, it is presumed that the shear band will continue to propagate under the influence of the general level of shear stress ($p/2$) in the system. The important characteristics predicted by Eqn. (21) are the effects of void size R and shape, m . These predictions are amenable to experimental investigation. It should be noted, however, that more rigorous analyses (not subject to the requirements that $R_0 \ll c$, $\tau_l \ll \tau \ll \tau_u$, and involving shear band thickening) may yield significantly reduced dependencies on the void size and shape. Also appreciable probabilistic influences based on the a priori size and spatial distribution of shear inhomogeneities are to be anticipated.

5. DISCUSSION AND CONCLUSIONS

Observations of kink band formation in composites and of shear band formation in epoxy indicates appreciable morphological similarity; suggesting that, at least in some instances, kink band formation is preceded by the development of a shear band within the matrix phase. The significant role of pre-existent inhomogeneities, particularly elliptical voids, in the initiation of kinks and shear bands has also been demonstrated. Notably, both types of bands tend to initiate preferentially at elliptical (rather than spherical) voids in a zone adjacent to the ends of the major axis.

An analysis of the elastic shear stresses generated around elliptical holes subject to axial compression indicates locations of appreciable stress concentration (depending upon the ellipticity) that closely coincide with the locations of shear band and kink initiation. Further, the trajectories of maximum shear stress are similar to the shear band trajectories. A shear band model based on the shear stress concentration levels around pre-existent inhomogeneities would thus appear pertinent.

A preliminary model has been proposed based on a concept that treats the shear band as an entity comparable to a mode II crack. This concept is based on a notion proposed by Bilby, Cottrell and Swinden and subsequently utilized by Argon. The model considers that a distribution of small stress inhomogeneities in the material interacts with the concentrated stress field around the voids to establish a critical condition for shear band formation. An approximate result (obtained by requiring a shear inhomogeneity of appropriate size to exist at the location of peak shear stress) indicates effects of void size and shape, and of the material's shear band resistance, on the critical applied stress for shear band formation. This result is amenable to direct experimental investigation.

ACKNOWLEDGMENT

This work was funded by the Office of Naval Research under contract no. N00014-79-C-0159.

REFERENCES

1. P.J. Goodnew, A.J. Clarke and J.E. Bailey, Materials Science and Eng., 17 (1975) 3.
2. G.A. Cooper and R.M. Mayer, Jnl. of Mater. Sci., 6 (1971) 60.
3. C.W. LeMaistre and R.J. Diefendorf, A symposium of the American Ceramic Society, Philadelphia (1971) 77.
4. J.L. Perry and D.F. Adams, Jnl. of Mater. Sci., 9 (1974) 1764.
5. D.F. Adams, Materials Science and Engineering, 17 (1975) 139.
6. M.G. Bader and M. Johnson, Composites, Mar., (1974) 58.
7. C.W. Weaver and J.G. Williams, Jnl. of Mater. Sci., 10 (1975) 1323.
8. S.V. Kulkarni, J.S. Rice and B.W. Rosen, Composites, Sept., (1975) 217.
9. C.R. Chaplin, Jnl. of Mater. Sci., 12 (1977) 347.
10. A.G. Evans and W.F. Adler, Acta Met., 26 (1978) 725.
11. B. Buciansky and J.C. Drucker, personal communication.
12. J.B.C. Wu and J.C.M. Li, Jnl. of Mater. Sci., 11 (1976) 434.
13. N.I. Muskhelishvili, Some Basic Problems of the Mathematical Theory of Elasticity.
14. S. Timoshenko and N.J. Goodier, Theory of Elasticity (McGraw-Hill, New York) 1951.
15. A.S. Argon, R.D. Andrews, J.A. Godrick and W. Whitney, Jnl. Appl. Phys., 39 (1968) 1899.
16. A.G. Fitzgerald and R. Engin., Jnl. of Mater. Sci., 9 (1974) 171.
17. T.E. Brady and G.S.Y. Yeh, Jnl. Appl. Phys., 42 (1971) 4622.
18. A.S. Argon, Polymeric Materials (Relationships Between Structure and Mechanical Behavior) 1975.
19. B.A. Bilby, A.H. Cottrell, F.R.S. and K.H. Swinden, Proc. Roy. Soc., A272 (1963) 304.
20. A.G. Evans, D.R. Biswas and R.M. Fulrath, Jnl. Amer. Ceram. Soc., 62 (1979) 101.

FIGURES

Fig. 1: A schematic diagram of kink formation from $\langle a \rangle$ fiber rotation instability at location of initial curvature $\langle b \rangle$ shear band.

Fig. 2: A schematic diagram of (a) constrained compressive tests and (b) flexure tests.

Fig. 3: A schematic diagram indicating steps of fabrication of glass/epoxy composites.

Fig. 4: Glass/epoxy composites with (a) notch parallel to compressive direction, (b) notch perpendicular to compressive direction and (c) a central cylindrical hole.

Fig. 5: A kink formed (a) between the fiber bundle and the matrix and (b) within the fiber bundles.

Fig. 6: A kink formed at the location of maximum compressive stress in flexure tests.

Fig. 7: Partially formed kink.

Fig. 8: Kinks and shear bands in glass/epoxy composites (Fig. 4).

Fig. 9: Kinks and shear bands in glass/epoxy composites.

Fig. 10: A schematic diagram of conformal transformation $Z = R(\xi + \frac{0.7}{\xi})$.

Fig. 11: The resultant shear stress and maximum shear stress trajectory from an elliptical hole ($m = 0.7$), diagram shows only quarter of the whole diagram.

Fig. 12: Same as Fig. 11 with $m = -0.8$.

Fig. 13: A plot of normalized stress intensity factor $\frac{K_{II}}{\hat{\tau}\sqrt{x_0}}$ as a function of the relative inhomogeneity size a_0/x_0

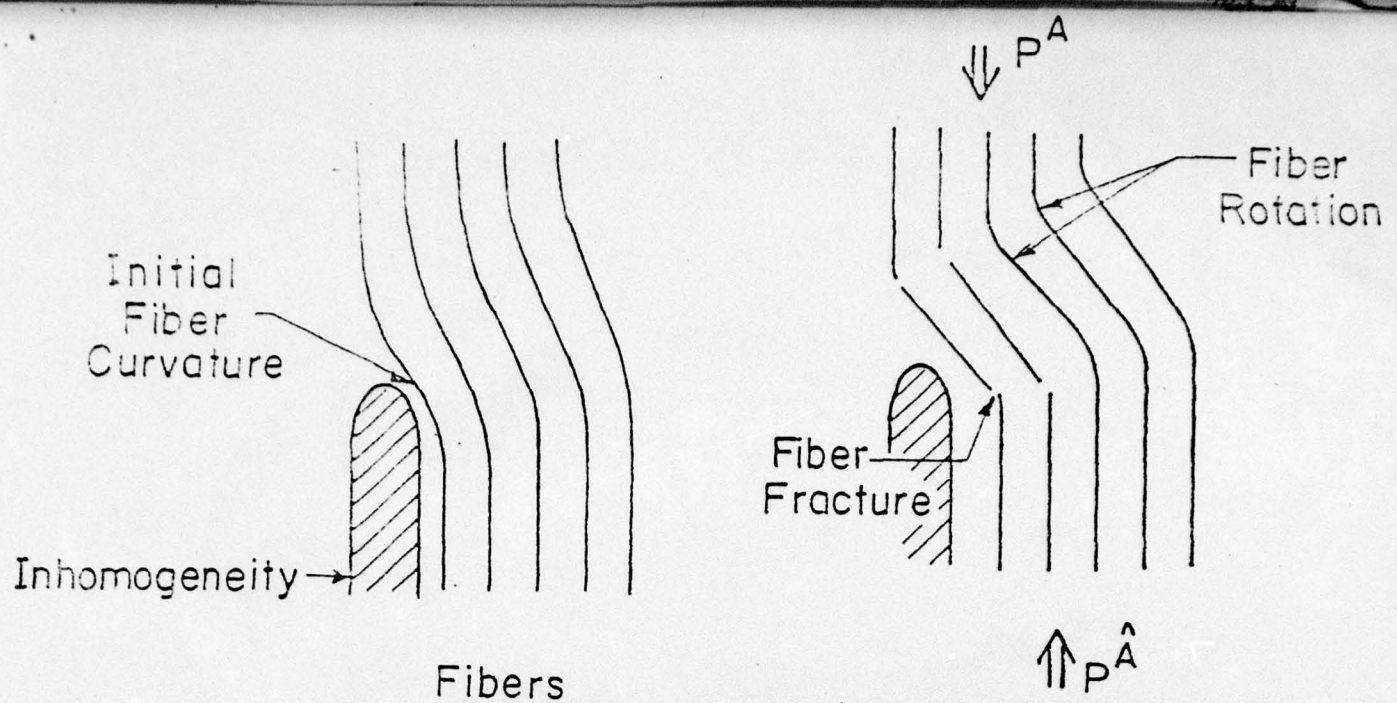
Tables for some fixed ϕ , the maximum shear stress $\rho\theta$ and the correspondent θ , θ' value.

Table 1 $m = 0.7$

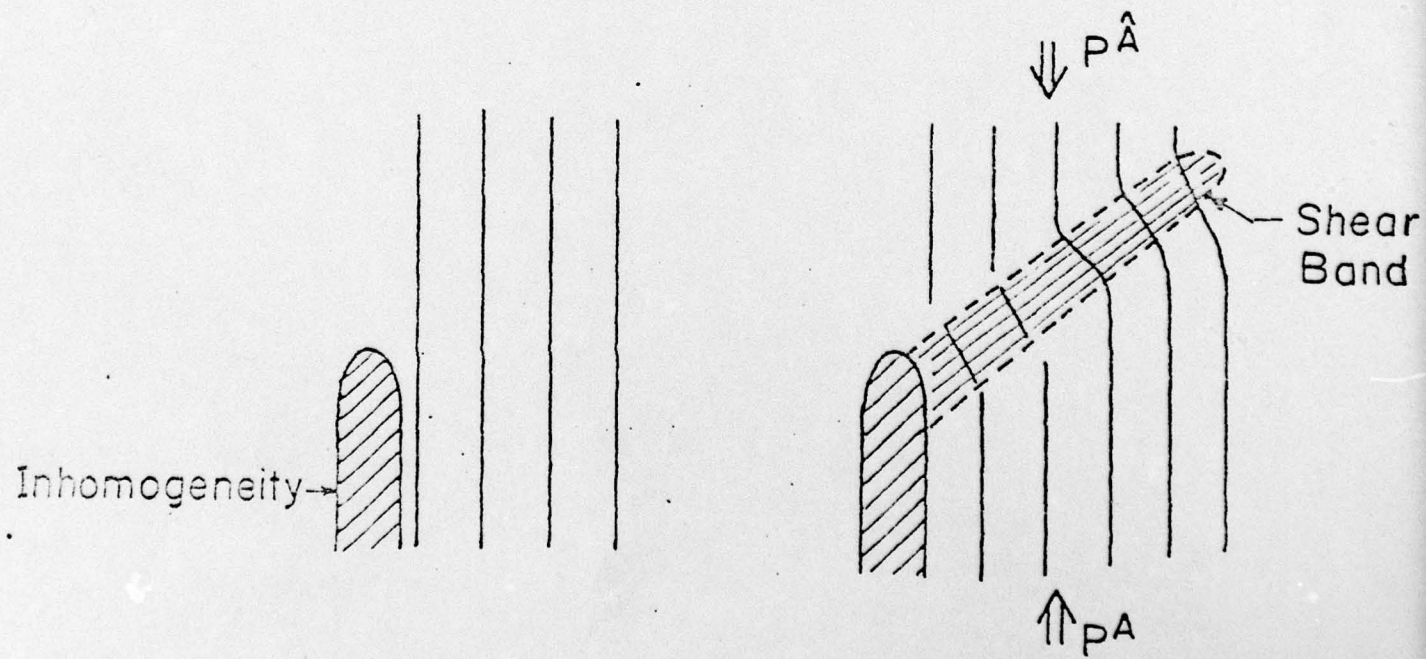
ρ	θ	θ'	$\rho\theta_{(\max)}/P$
1.05	9°	2°	-0.25
1.1	11°	3°	-0.37
1.2	16°	6°	-0.46
1.5	25°	14°	-0.54
2	34°	25°	-0.545
3	40°	36°	-0.53
4	43°	40.5°	-0.52
5	44.5°	43°	-0.52

Table 2 $m = -0.8$

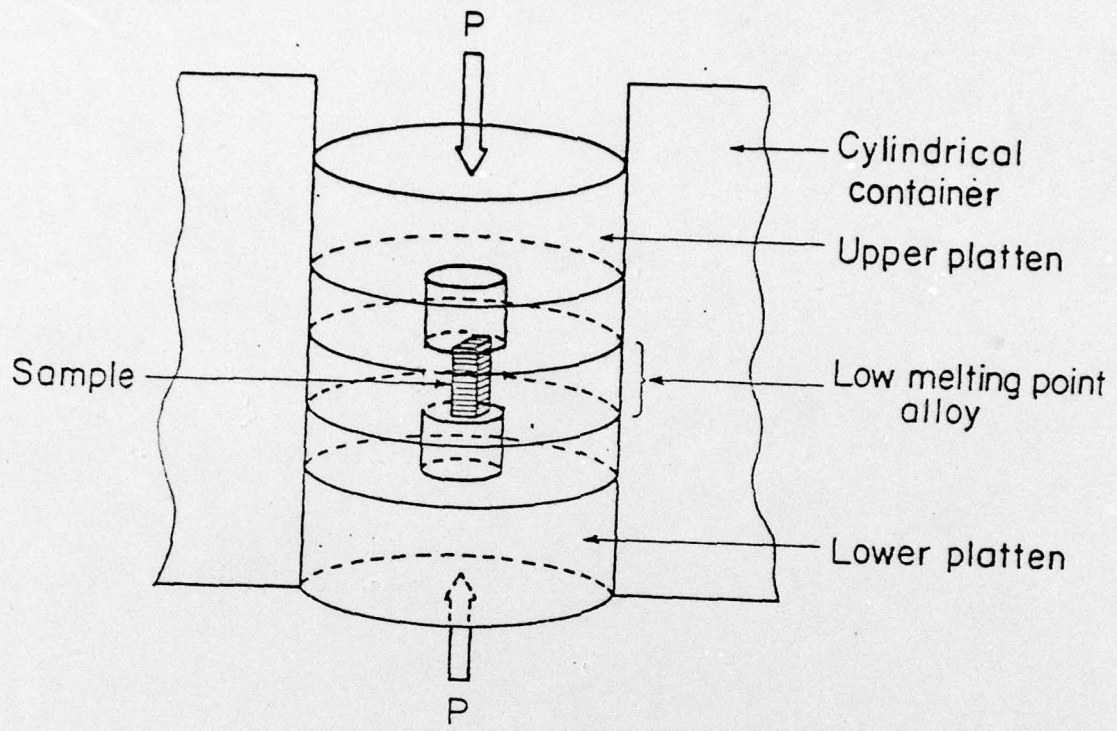
ρ	θ	θ'	$\rho\theta_{(\max)}/P$
1.05	85°	89°	-1.32
1.1	83°	88.6°	-1.45
1.2	79°	87°	-1.35
1.3	77°	85°	-1.2
1.5	71°	81°	-1
1.7	65°	75°	-0.85
2	60°	70°	-0.8
3	51°	56°	-0.65
4	47°	50°	-0.6
5	45°	47°	-0.55



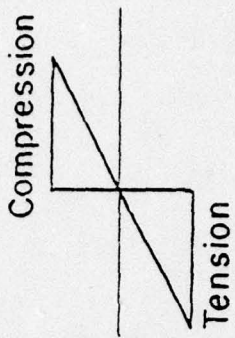
a) Fiber Rotation Instability at Location of Initial Curvature



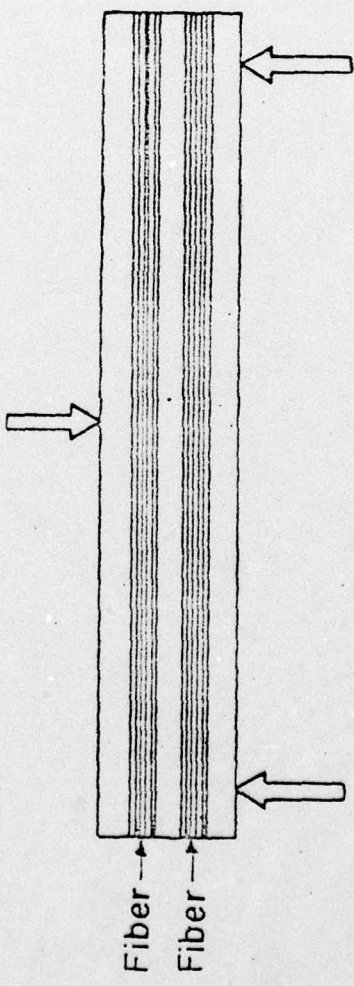
b) Kinking at Shear Band

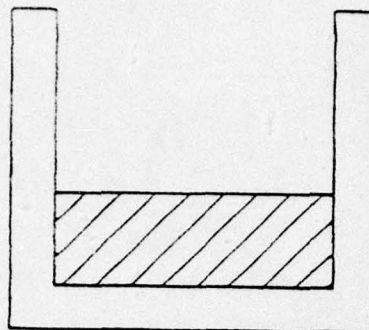


XBL 7910-7174

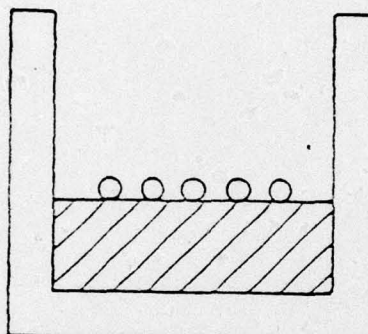


XBL 7910-7175

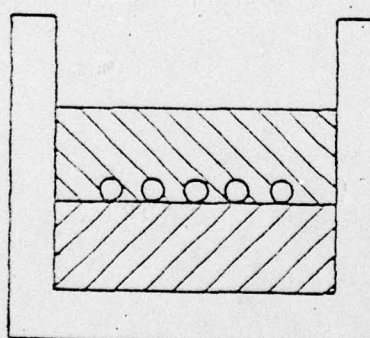




Step 1
First epoxy layer
vacuum treatment

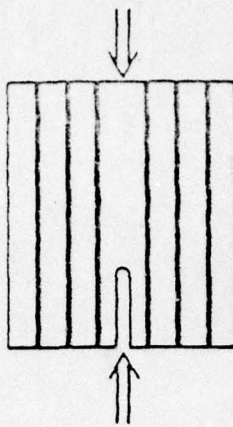


Step 2
Fiber arrangement

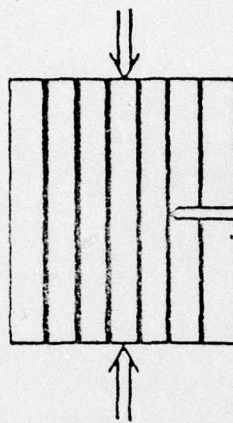


Step 3
Second epoxy layer
vacuum treatment

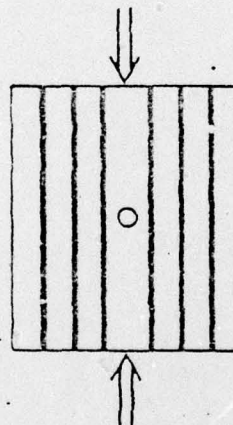
XBL 7910-7 176



(a) Notch parallel to compressive direction

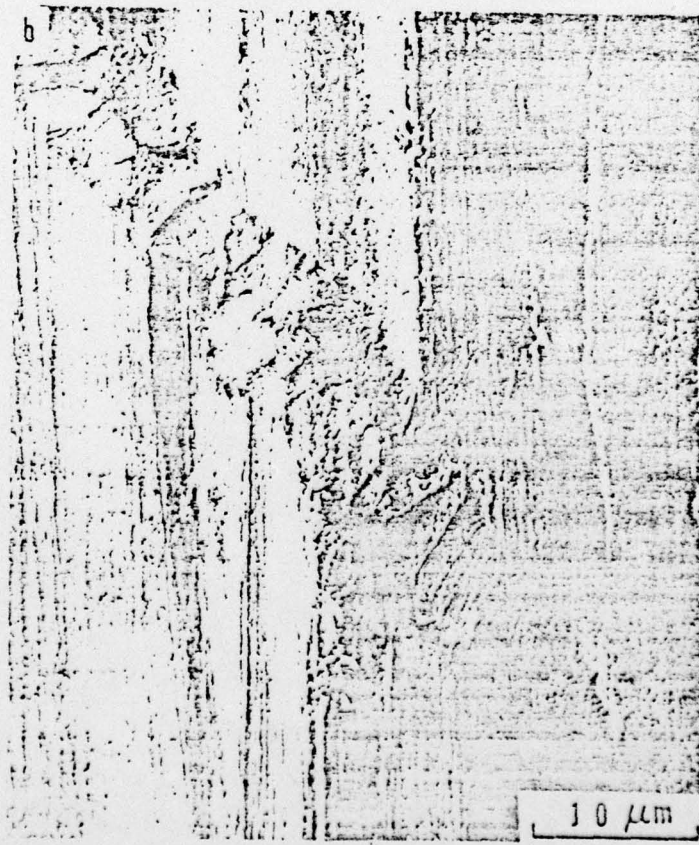
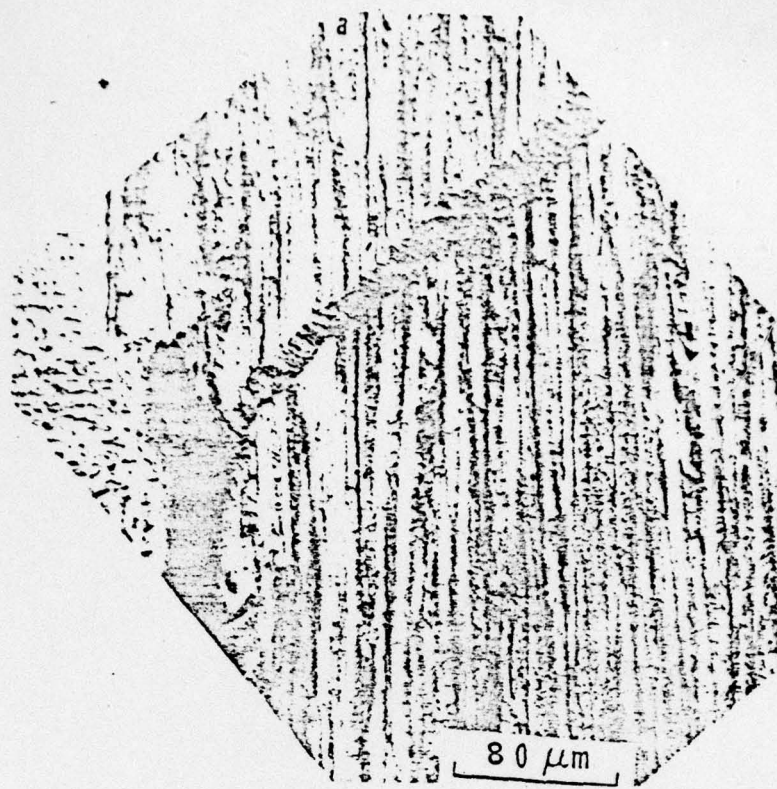


(b) Notch perpendicular to compressive direction

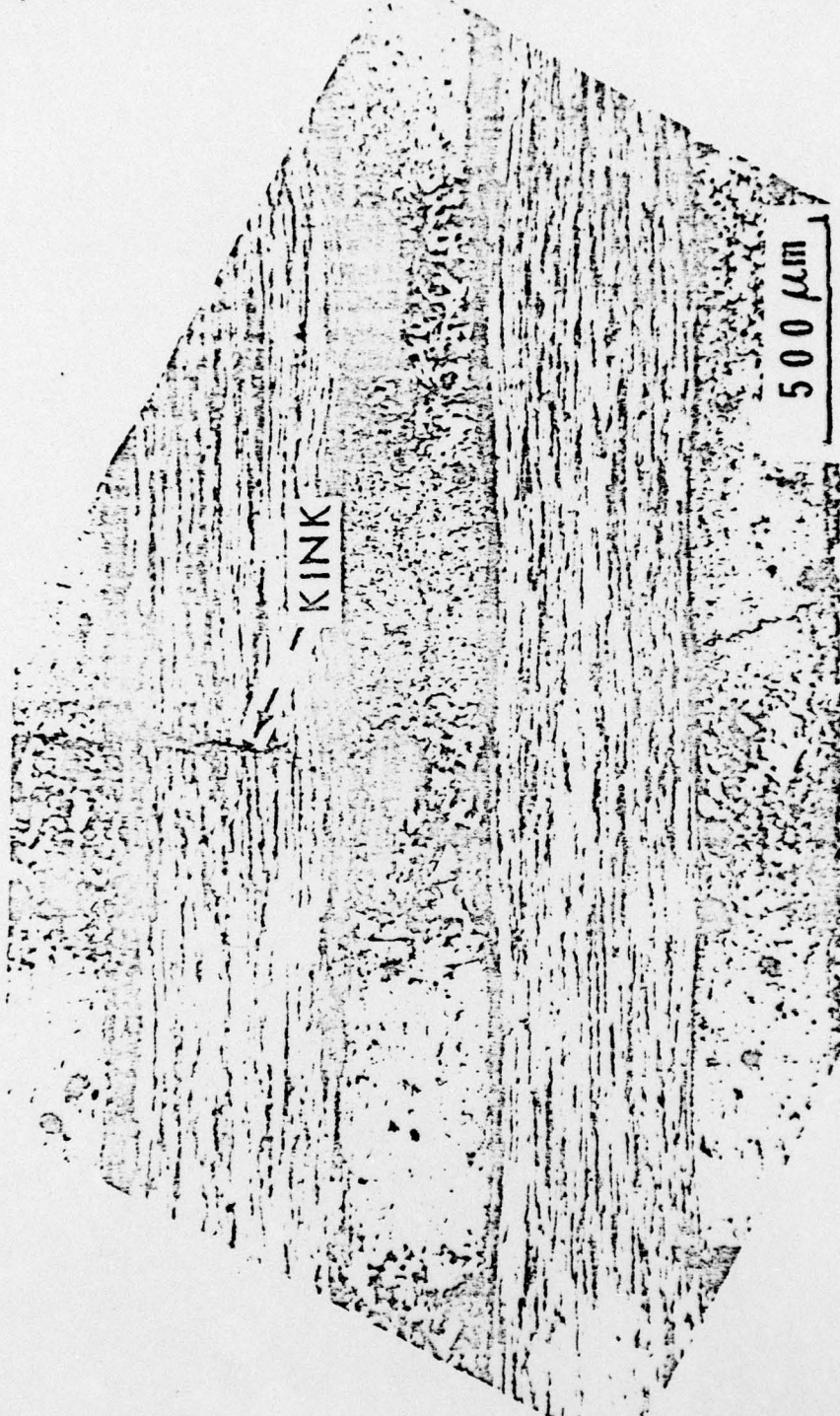


(c) A central cylindrical hole in the sample

XBL7910-7177



P

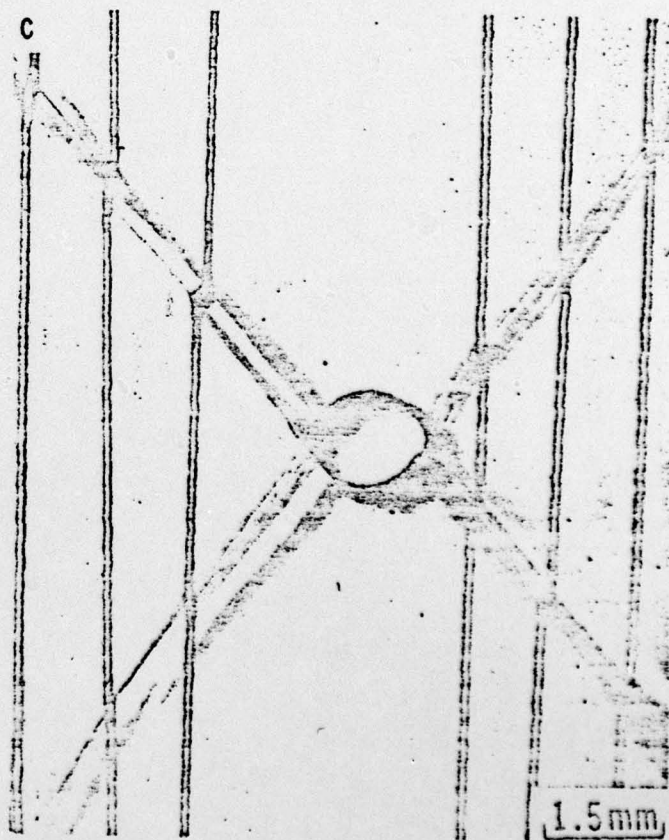
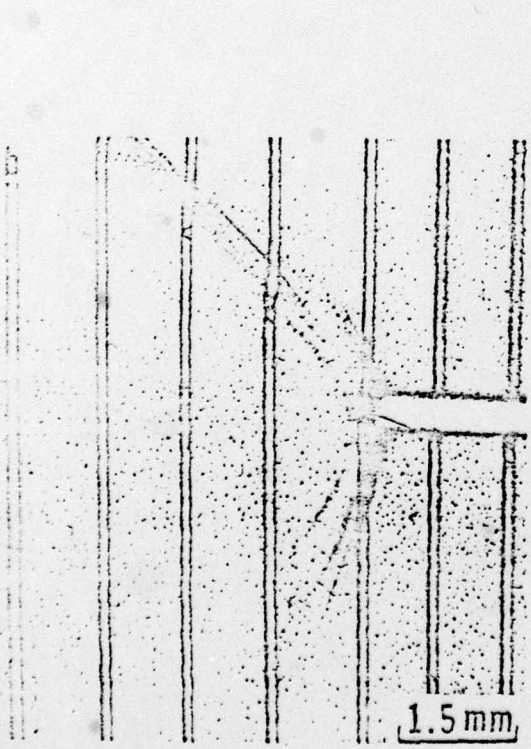
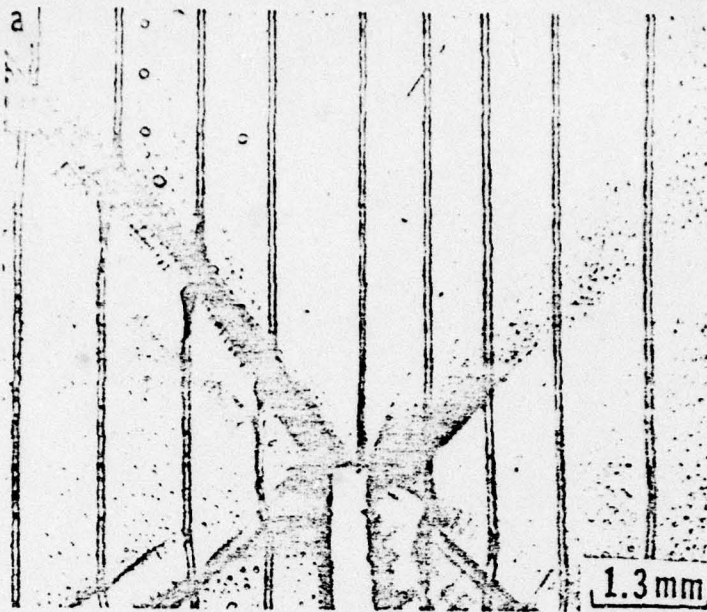


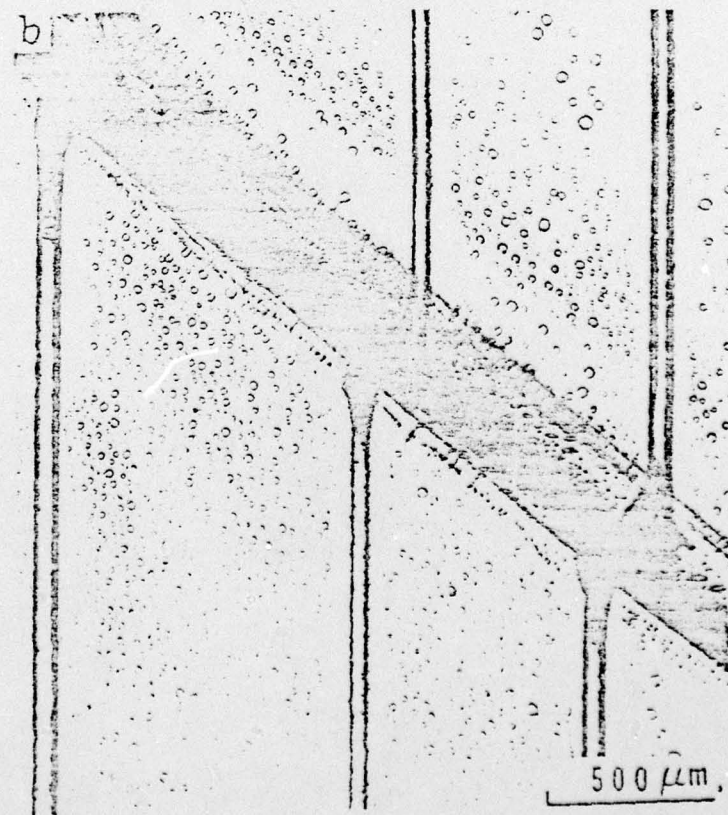
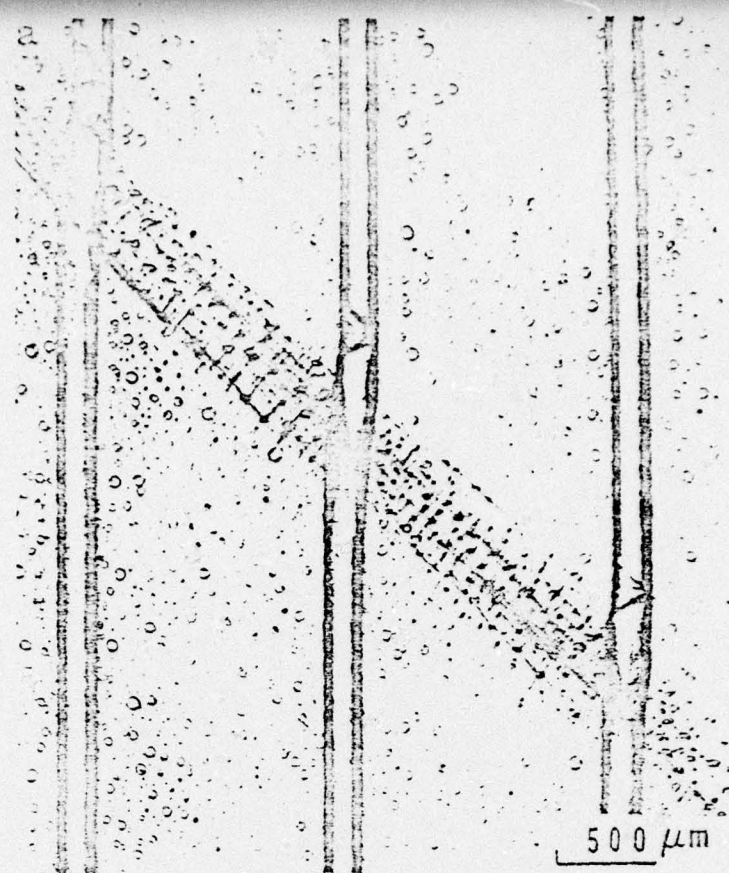
P/2

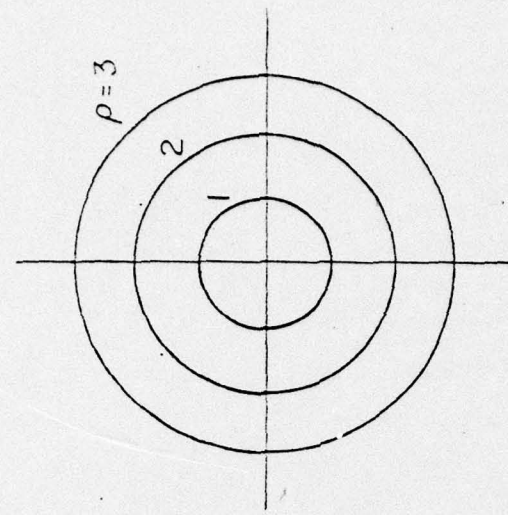
P/2

CRACK TIP

20 μ m

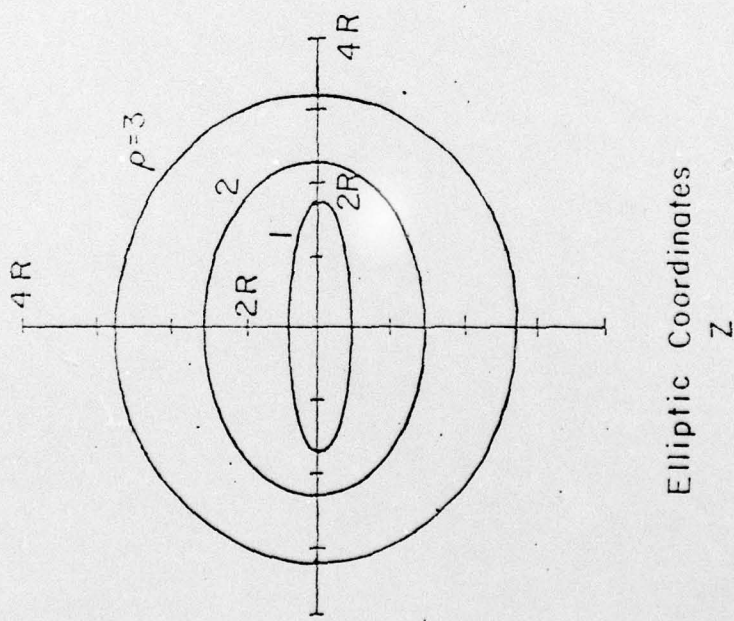






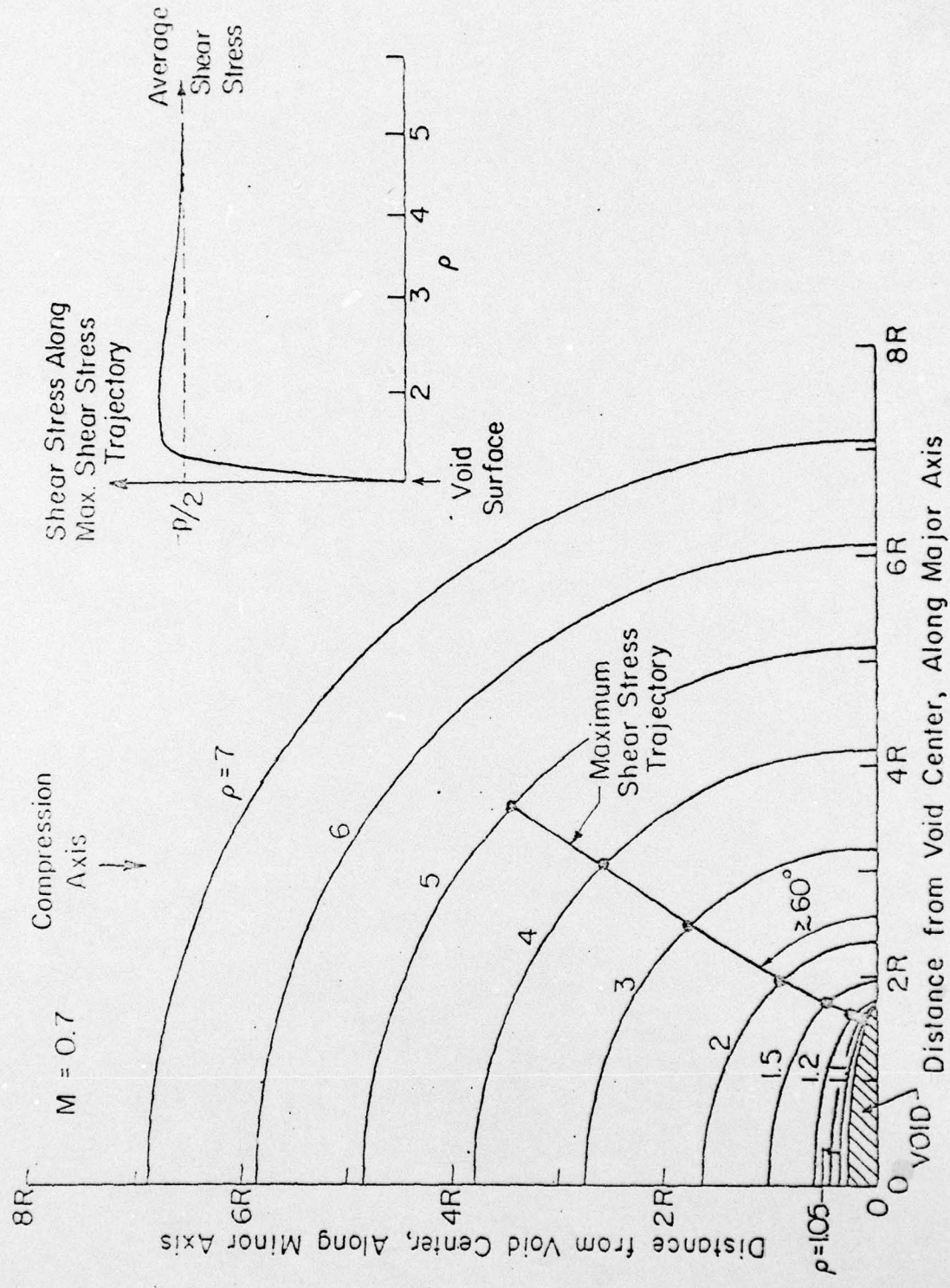
Equivalent Circular Coordinates
 $\omega(\xi)$

$M = 0.7$

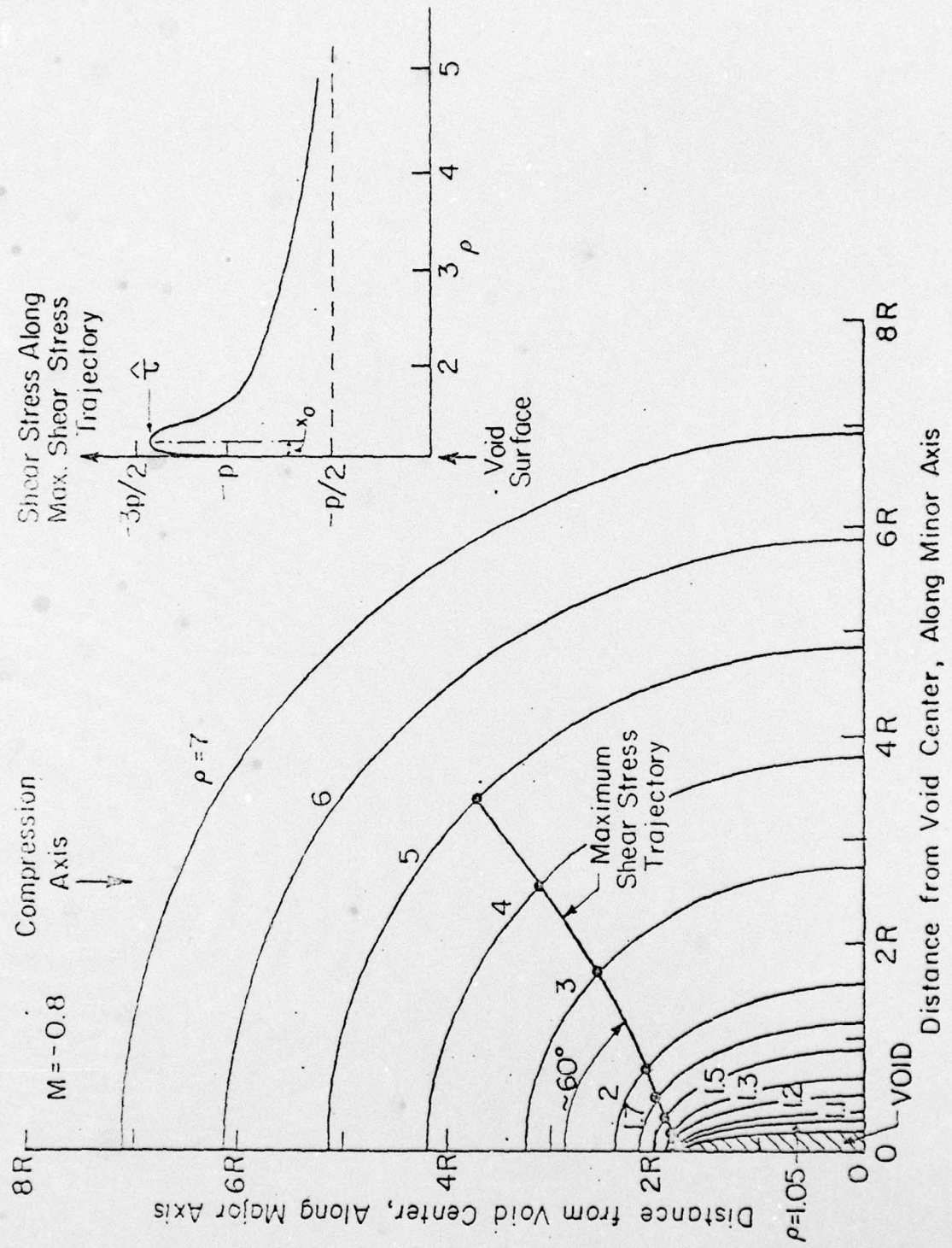


Elliptic Coordinates
 $\omega(\xi)$

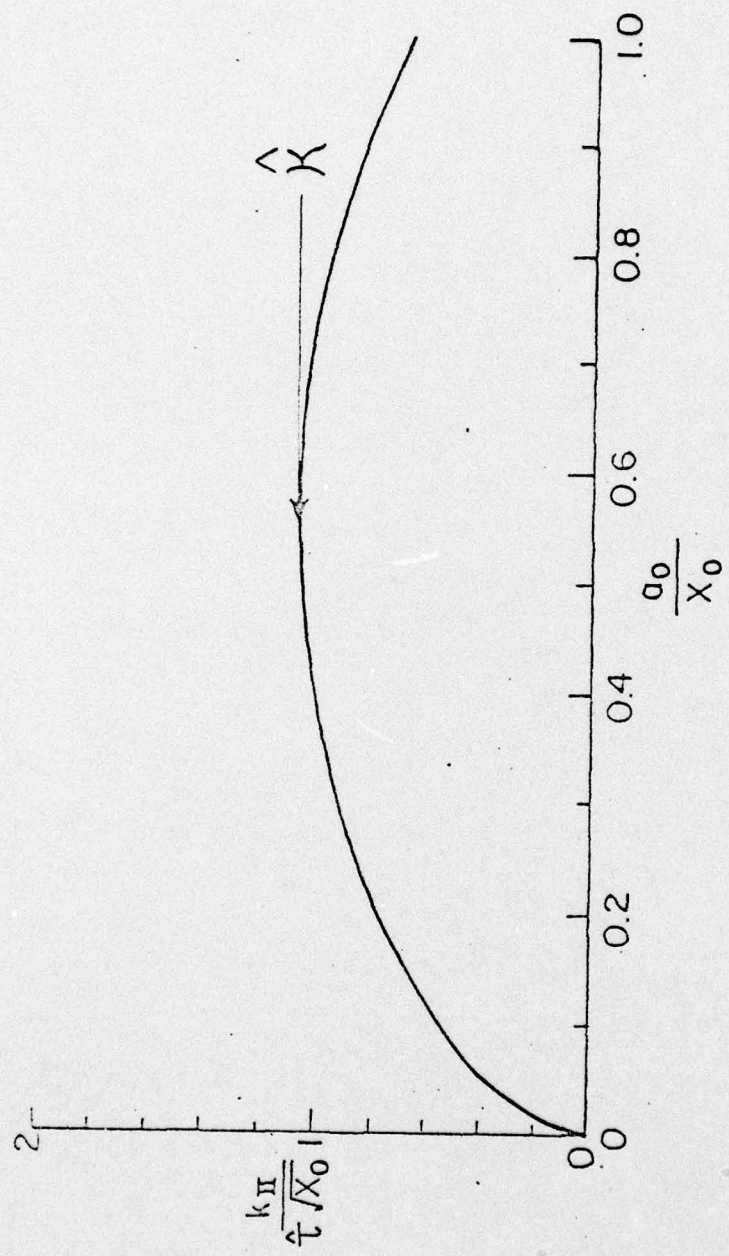
XBL 7910-7173



XBL7910-7179



XBL7910-7180



XBL7910-7178